PHYSICAL REVIEW D **88**, 032005 (2013)

Study of exclusive $B \to X_u \ell \nu$ decays and extraction of $|V_{ub}|$ using full reconstruction tagging at the Belle experiment

A. Sibidanov,[52] K. E. Varvell,[52] I. Adachi,[11] H. Aihara,[58] D. M. Asner,[45] V. Aulchenko,[3] T. Aushev,[20] A. M. Bakich,[52] A. Bala,[46] A. Bozek,[40] M. Bračko,[30,21] T. E. Browder,[10] V. Chekelian,[31] P. Chen,[39] B. G. Cheon,[9] K. Chilikin,[20] R. Chistov,[20] I.-S. Cho,[65] K. Cho,[24] V. Chobanova,[31] Y. Choi,[51] D. Cinabro,[63] J. Dalseno,[31,54] M. Danilov,[20,33] J. Dingfelder,[2] Z. Doležal,[4] Z. Drásal,[4] A. Drutskoy,[20,33] D. Dutta,[14] S. Eidelman,[3] D. Epifanov,[58] H. Farhat,[63] J. E. Fast,[45] T. Ferber,[6] A. Frey,[66] V. Gaur,[53] S. Ganguly,[63] R. Gillard,[63] Y. M. Goh,[9] B. Golob,[28,21] J. Haba,[11] H. Hayashii,[37] Y. Hoshi,[56] W.-S. Hou,[39] H. J. Hyun,[26] T. Iijima,[36,35] A. Ishikawa,[57] R. Itoh,[11] Y. Iwasaki,[11] T. Julius,[32] D. H. Kah,[26] J. H. Kang,[65] T. Kawasaki,[42] C. Kiesling,[31] D. Y. Kim,[50] H. J. Kim,[26] J. B. Kim,[25] J. H. Kim,[24] K. T. Kim,[25] Y. J. Kim,[24] J. Klucar,[21] B. R. Ko,[25] P. Kodyš,[4] S. Korpar,[30,21] P. Križan,[28,21] P. Krokovny,[3] B. Kronenbitter,[23] T. Kuhr,[23] A. Kuzmin,[3] Y.-J. Kwon,[65] S.-H. Lee,[25] J. Li,[49] Y. Li,[62] J. Libby,[15] Y. Liu,[5] D. Liventsev,[11] P. Lukin,[3] D. Matvienko,[3] K. Miyabayashi,[37] H. Miyata,[42] G. B. Mohanty,[53] A. Moll,[31,54] R. Mussa,[19] Y. Nagasaka,[12] E. Nakano,[44] M. Nakao,[11] Z. Natkaniec,[40] M. Nayak,[15] E. Nedelkovska,[31] C. Ng,[58] N. K. Nisar,[53] S. Nishida,[11] O. Nitoh,[61] T. Nozaki,[11] S. Ogawa,[55] S. Okuno,[22] S. L. Olsen,[49] C. Oswald,[2] H. Park,[26] H. K. Park,[26] T. K. Pedlar,[29] R. Pestotnik,[21] M. Petrič,[21] L. E. Piilonen,[62] M. Ritter,[31] M. Röhrken,[23] A. Rostomyan,[6] S. Ryu,[49] H. Sahoo,[10] T. Saito,[57] Y. Sakai,[11] S. Sandilya,[53] L. Santelj,[21] T. Sanuki,[57] Y. Sato,[57] V. Savinov,[47] O. Schneider,[27] G. Schnell,[1,13] C. Schwanda,[17] K. Senyo,[64] O. Seon,[35] M. E. Sevior,[32] M. Shapkin,[18] V. Shebalin,[3] C. P. Shen,[35] T.-A. Shibata,[59] J.-G. Shiu,[39] F. Simon,[31,54] P. Smerkol,[21] Y.-S. Sohn,[65] E. Solovieva,[20] S. Stanič,[43] M. Starič,[21] M. Steder,[6] M. Sumihama,[8] K. Sumisawa,[11] T. Sumiyoshi,[60] G. Tatishvili,[45] Y. Teramoto,[44] K. Trabelsi,[11] T. Tsuboyama,[11] M. Uchida,[59] S. Uehara,[11] T. Uglov,[20,34] Y. Unno,[9] S. Uno,[11] P. Urquijo,[2] Y. Ushiroda,[11] S. E. Vahsen,[10] C. Van Hulse,[1] P. Vanhoefer,[31] G. Varner,[10] V. Vorobyev,[3] M. N. Wagner,[7] C. H. Wang,[38] P. Wang,[16] M. Watanabe,[42] Y. Watanabe,[22] K. M. Williams,[62] E. Won,[25] B. D. Yabsley,[52] Y. Yamashita,[41] S. Yashchenko,[6] Y. Yook,[65] Z. P. Zhang,[48] V. Zhilich,[3] V. Zhulanov,[3] and A. Zupanc[23]

(Belle Collaboration)

[1]*University of the Basque Country UPV/EHU, 48080 Bilbao*
[2]*University of Bonn, 53115 Bonn*
[3]*Budker Institute of Nuclear Physics SB RAS and Novosibirsk State University, Novosibirsk 630090*
[4]*Faculty of Mathematics and Physics, Charles University, 121 16 Prague*
[5]*University of Cincinnati, Cincinnati, Ohio 45221*
[6]*Deutsches Elektronen–Synchrotron, 22607 Hamburg*
[7]*Justus-Liebig-Universität Gießen, 35392 Gießen*
[8]*Gifu University, Gifu 501-1193*
[9]*Hanyang University, Seoul 133-791*
[10]*University of Hawaii, Honolulu, Hawaii 96822*
[11]*High Energy Accelerator Research Organization (KEK), Tsukuba 305-0801*
[12]*Hiroshima Institute of Technology, Hiroshima 731-5193*
[13]*Ikerbasque, 48011 Bilbao*
[14]*Indian Institute of Technology Guwahati, Assam 781039*
[15]*Indian Institute of Technology Madras, Chennai 600036*
[16]*Institute of High Energy Physics, Chinese Academy of Sciences, Beijing 100049*
[17]*Institute of High Energy Physics, Vienna 1050*
[18]*Institute for High Energy Physics, Protvino 142281*
[19]*INFN - Sezione di Torino, 10125 Torino*
[20]*Institute for Theoretical and Experimental Physics, Moscow 117218*
[21]*J. Stefan Institute, 1000 Ljubljana*
[22]*Kanagawa University, Yokohama 221-8686*
[23]*Institut für Experimentelle Kernphysik, Karlsruher Institut für Technologie, 76131 Karlsruhe*
[24]*Korea Institute of Science and Technology Information, Daejeon 305-806*
[25]*Korea University, Seoul 136-713*
[26]*Kyungpook National University, Daegu 702-701*
[27]*École Polytechnique Fédérale de Lausanne (EPFL), Lausanne 1015*
[28]*Faculty of Mathematics and Physics, University of Ljubljana, 1000 Ljubljana*
[29]*Luther College, Decorah, Iowa 52101*
[30]*University of Maribor, 2000 Maribor*
[31]*Max-Planck-Institut für Physik, 80805 München*

1550-7998/2013/88(3)/032005(25)

[32]*School of Physics, University of Melbourne, Victoria 3010*
[33]*Moscow Physical Engineering Institute, Moscow 115409*
[34]*Moscow Institute of Physics and Technology, Moscow Region 141700*
[35]*Graduate School of Science, Nagoya University, Nagoya 464-8602*
[36]*Kobayashi-Maskawa Institute, Nagoya University, Nagoya 464-8602*
[37]*Nara Women's University, Nara 630-8506*
[38]*National United University, Miao Li 36003*
[39]*Department of Physics, National Taiwan University, Taipei 10617*
[40]*H. Niewodniczanski Institute of Nuclear Physics, Krakow 31-342*
[41]*Nippon Dental University, Niigata 951-8580*
[42]*Niigata University, Niigata 950-2181*
[43]*University of Nova Gorica, 5000 Nova Gorica*
[44]*Osaka City University, Osaka 558-8585*
[45]*Pacific Northwest National Laboratory, Richland, Washington 99352*
[46]*Panjab University, Chandigarh 160014*
[47]*University of Pittsburgh, Pittsburgh, Pennsylvania 15260*
[48]*University of Science and Technology of China, Hefei 230026*
[49]*Seoul National University, Seoul 151-742*
[50]*Soongsil University, Seoul 156-743*
[51]*Sungkyunkwan University, Suwon 440-746*
[52]*School of Physics, University of Sydney, NSW 2006*
[53]*Tata Institute of Fundamental Research, Mumbai 400005*
[54]*Excellence Cluster Universe, Technische Universität München, 85748 Garching*
[55]*Toho University, Funabashi 274-8510*
[56]*Tohoku Gakuin University, Tagajo 985-8537*
[57]*Tohoku University, Sendai 980-8578*
[58]*Department of Physics, University of Tokyo, Tokyo 113-0033*
[59]*Tokyo Institute of Technology, Tokyo 152-8550*
[60]*Tokyo Metropolitan University, Tokyo 192-0397*
[61]*Tokyo University of Agriculture and Technology, Tokyo 184-8588*
[62]*CNP, Virginia Polytechnic Institute and State University, Blacksburg, Virginia 24061*
[63]*Wayne State University, Detroit, Michigan 48202*
[64]*Yamagata University, Yamagata 990-8560*
[65]*Yonsei University, Seoul 120-749*
[66]*II. Physikalisches Institut, Georg-August-Universität Göttingen, 37073 Göttingen*

(Received 12 June 2013; published 7 August 2013)

We report the results of a study of the exclusive semileptonic decays $B^- \to \pi^0\ell^-\bar{\nu}_\ell$, $\bar{B}^0 \to \pi^+\ell^-\bar{\nu}_\ell$, $B^- \to \rho^0\ell^-\bar{\nu}_\ell$, $\bar{B}^0 \to \rho^+\ell^-\bar{\nu}_\ell$ and $B^- \to \omega\ell^-\bar{\nu}_\ell$, where ℓ represents an electron or a muon. The events are tagged by fully reconstructing a second B meson in the event in a hadronic decay mode. The measured branching fractions are $\mathcal{B}(B^- \to \pi^0\ell^-\bar{\nu}_\ell) = (0.80 \pm 0.08 \pm 0.04) \times 10^{-4}$, $\mathcal{B}(\bar{B}^0 \to \pi^+\ell^-\bar{\nu}_\ell) = (1.49 \pm 0.09 \pm 0.07) \times 10^{-4}$, $\mathcal{B}(B^- \to \rho^0\ell^-\bar{\nu}_\ell) = (1.83 \pm 0.10 \pm 0.10) \times 10^{-4}$, $\mathcal{B}(\bar{B}^0 \to \rho^+\ell^-\bar{\nu}_\ell) = (3.22 \pm 0.27 \pm 0.24) \times 10^{-4}$, and $\mathcal{B}(B^- \to \omega\ell^-\bar{\nu}_\ell) = (1.07 \pm 0.16 \pm 0.07) \times 10^{-4}$, where the first error is statistical and the second one is systematic. The obtained branching fractions are inclusive of soft photon emission. We also determine the branching fractions as a function of the 4-momentum transfer squared to the leptonic system $q^2 = (p_\ell + p_\nu)^2$, where p_ℓ and p_ν are the lepton and neutrino 4-momenta, respectively. Using the pion modes, a recent light cone sum rule calculation, lattice QCD results and a model-independent description of the hadronic form factor, a value of the Cabibbo-Kobayashi-Maskawa matrix element $|V_{ub}| = (3.52 \pm 0.29) \times 10^{-3}$ is extracted. A structure in the two-pion invariant mass distribution near 1.3 GeV/c^2, which might be dominated by the decay $B^- \to f_2(1270)\ell^-\bar{\nu}_\ell$, $f_2 \to \pi^+\pi^-$, is seen. These results are obtained from a 711 fb^{-1} data sample that contains 772×10^6 $B\bar{B}$ pairs, collected near the $\Upsilon(4S)$ resonance with the Belle detector at the KEKB asymmetric-energy e^+e^- collider.

DOI: 10.1103/PhysRevD.88.032005 PACS numbers: 13.20.−v, 12.15.Hh, 12.38.Gc, 14.40.Nd

I. INTRODUCTION

The Standard Model (SM) of particle physics contains a number of parameters whose values are not predicted by theory and must therefore be measured by experiment. In the quark sector, the elements of the Cabibbo-Kobayashi-Maskawa (CKM) matrix [1] determine the rates of the weak transitions between quark flavors, and precision measurements of their values are desirable. In particular, in the context of B-meson decays, there is currently much experimental and theoretical effort to test the consistency of the well-known CKM unitarity triangle (UT).

The UT angle ϕ_1 [2], characterizing indirect *CP* violation in $b \to c\bar{c}s$ transitions, was first observed to be nonzero in 2001 [3], and $\sin 2\phi_1$ is now known to a precision of better than 3% [4]. This makes a corresponding precision measurement of the length of the side of the unitarity triangle opposite ϕ_1 particularly important as a consistency check of the SM picture. The length of this side is determined to a good approximation by the ratio of the magnitudes of two CKM matrix elements, $|V_{ub}/V_{cb}|$. Both can be measured using exclusive semileptonic B-meson decays. Using charmed semileptonic decays, the precision to which $|V_{cb}|$ has been determined is 2%–3% [5]. In comparison, $|V_{ub}|$, which can be measured using charmless semileptonic decays, is poorly known. Both inclusive and exclusive methods of measuring $|V_{ub}|$ have been pursued, with the results of the two approaches being in some tension [6]. It is the aim of an ongoing program at the B factories to improve the precision of these measurements, in order to provide a more stringent comparison of exclusive and inclusive results, which have somewhat different experimental and theoretical uncertainties, and to provide a sharp consistency test with the value of $\sin 2\phi_1$.

Measurements of branching fractions for exclusive $\bar{B} \to X_u \ell^- \bar{\nu}_\ell$ decays, where X_u denotes a light meson containing a u quark and ℓ an electron or muon, have been reported by the CLEO [7], *BABAR* [8–12] and Belle [13–15] collaborations. Three methods of identifying signal candidates have been employed in these studies. In untagged analyses, the missing energy and momentum of the whole event are used to reconstruct the neutrino from the signal semileptonic decay. Semileptonic tagging involves partial reconstruction of a $B \to D^{(*)}\ell\nu$ decay as the tagging mode. In this case, two neutrinos are present in the event and the kinematics cannot be fully constrained. In full reconstruction tagging, a hadronically decaying B meson is reconstructed, against which the signal decay recoils.

In this article, we present measurements of the total and partial branching fractions for the exclusive semileptonic decays $\bar{B}^0 \to \pi^+ \ell^- \bar{\nu}_\ell$, $B^- \to \pi^0 \ell^- \bar{\nu}_\ell$, $\bar{B}^0 \to \rho^+ \ell^- \bar{\nu}_\ell$, $B^- \to \rho^0 \ell^- \bar{\nu}_\ell$ and $B^- \to \omega \ell^- \bar{\nu}_\ell$ [16] using the full reconstruction tagging technique. The measurement is based on a 711 fb^{-1} data sample that contains $(772 \pm 11) \times 10^6$ $B\bar{B}$ pairs, collected with the Belle detector at the KEKB asymmetric-energy e^+e^- (3.5 on 8 GeV) collider [17] operating at the $\Upsilon(4S)$ resonance.

The Belle detector is a large-solid-angle magnetic spectrometer that consists of a silicon vertex detector (SVD), a 50-layer central drift chamber (CDC), an array of aerogel threshold Cherenkov counters (ACC), a barrel-like arrangement of time-of-flight scintillation counters (TOF) and an electromagnetic calorimeter comprised of CsI(Tl) crystals (ECL) located inside a superconducting solenoid coil that provides a 1.5 T magnetic field. An iron flux-return yoke located outside of the coil is instrumented to detect K_L^0 mesons and to identify muons (KLM). The detector is described in detail elsewhere [18]. Two inner detector configurations were used. A 2.0 cm beampipe and a 3-layer silicon vertex detector were used for the first sample of 152×10^6 $B\bar{B}$ pairs, while a 1.5 cm beampipe, a 4-layer silicon detector and a small-cell inner drift chamber were used to record the remaining 620×10^6 $B\bar{B}$ pairs [19].

Recently, a new reconstruction procedure for B-meson hadronic decays based on the NeuroBayes neural network package [20] has been introduced in Belle. This procedure reconstructs B mesons in more than 1100 exclusive hadronic decay channels. Compared to the previous cut-based algorithm, it offers roughly a factor of 2 efficiency gain and about 2.1×10^6 (1.4×10^6) fully reconstructed charged (neutral) B-meson decays within the data sample collected at the $\Upsilon(4S)$ resonance.

II. DIFFERENTIAL DECAY RATES

The decay rate for the process $B \to f_1 f_2 \ldots$, where the f_i represent final state particles, is given by

$$\mathrm{d}\Gamma(B \to f_1 f_2 \ldots) = \frac{1}{2m_B} |\mathcal{M}(B \to f_1 f_2 \ldots)|^2 \mathrm{d}\Pi, \quad (1)$$

where m_B is the mass of the B meson, $\mathcal{M}$ is the matrix element for the decay,

$$\mathrm{d}\Pi = (2\pi)^4 \delta^{(4)}\Big(p_B - \sum_i p_i\Big) \prod_i \frac{\mathrm{d}^3 \vec{p}_i}{(2\pi)^3 2E_i} \quad (2)$$

is the total decay phase space element, p_B is the 4-vector of the parent B meson and $p_i = (E_i, \vec{p}_i)$ are the 4-vectors of the final state particles f_i.

The matrix element for weak semileptonic B-meson decays at first order can be written as

$$\mathcal{M}(\bar{B} \to X_q \ell^- \bar{\nu}_\ell) = \frac{G_F}{\sqrt{2}} V_{qb} L^\mu H_\mu, \quad (3)$$

where G_F is the Fermi constant, V_{qb} is the element of the CKM matrix corresponding to the $b \to q$ transition, $L^\mu = \bar{u}_\ell \gamma^\mu (1 - \gamma^5) v_\nu$ is the leptonic current and H_μ is the hadronic current, which depends on the particular hadronic final state. More details about the subsequent formulas can be found elsewhere [21].

A. The $\bar{B} \to \pi \ell^- \bar{\nu}_\ell$ decay

We can parametrize the hadronic current for the $\bar{B} \to \pi \ell^- \bar{\nu}_\ell$ decay as

$$\begin{aligned} H_\mu &= \langle \pi(p_\pi)|V_\mu|B(p_B)\rangle \\ &= f_+(q^2)\left(p_B + p_\pi - q\frac{m_B^2 - m_\pi^2}{q^2}\right)_\mu \\ &\quad + f_0(q^2)\frac{m_B^2 - m_\pi^2}{q^2}q_\mu, \end{aligned} \tag{4}$$

where $q = p_B - p_\pi = p_W = p_\ell + p_\nu$ is the 4-momentum transferred to the leptonic system, $f_+(q^2)$ is a vector form factor, and $f_0(q^2)$ is a scalar form factor; we use $f_+(0) \equiv f_0(0)$ to avoid a kinematic singularity at $q^2 = 0$.

The differential decay rate for the process involving pseudoscalar mesons is written as

$$\begin{aligned} &\frac{\mathrm{d}\Gamma}{\mathrm{d}q^2}(\bar{B} \to \pi\ell^-\bar{\nu}_\ell) \\ &\quad = \frac{G_F^2|V_{ub}|^2}{24\pi^3 m_B^2 q^4}(q^2 - m_\ell^2)^2|\vec{p}_\pi| \\ &\quad\quad \times\left[\left(1 + \frac{m_\ell^2}{2q^2}\right)m_B^2|\vec{p}_\pi|^2|f_+(q^2)|^2\right. \\ &\quad\quad \left. + \frac{3m_\ell^2}{8q^2}(m_B^2 - m_\pi^2)^2|f_0(q^2)|^2\right], \end{aligned} \tag{5}$$

where $|\vec{p}_\pi|$ is the magnitude of the pion momentum in the B rest frame. For light leptons (e and μ), we can neglect terms proportional to m_ℓ^2 so that only $f_+(q^2)$ is relevant:

$$\frac{\mathrm{d}\Gamma}{\mathrm{d}q^2} = \frac{G_F^2}{24\pi^3}|V_{ub}|^2|f_+(q^2)|^2|\vec{p}_\pi|^3. \tag{6}$$

B. The $\bar{B} \to \rho\ell^-\bar{\nu}_\ell$ and $B^- \to \omega\ell^-\bar{\nu}_\ell$ decays

For semileptonic decays with vector mesons in the final state, i.e., ρ or ω, we can define the hadronic current with four dimensionless form factors:

$$\begin{aligned} H_\mu &= \langle V(p)|(V-A)_\mu|B(p_B)\rangle = -i\epsilon_\mu^*(m_B + m_V)A_1^V(q^2) \\ &\quad + i(p_B + p)_\mu(\epsilon^* p_B)\frac{A_2^V(q^2)}{m_B + m_V} \\ &\quad + iq_\mu(\epsilon^* p_B)\frac{2m_V}{q^2}(A_3^V(q^2) - A_0^V(q^2)) \\ &\quad + \epsilon_{\mu\nu\rho\sigma}\epsilon^{*\nu}p_B^\rho p^\sigma\frac{2V^V(q^2)}{m_B + m_V}, \end{aligned} \tag{7}$$

with the exact relations among the form factors

$$A_3^V(q^2) = \frac{m_B + m_V}{2m_V}A_1^V(q^2) - \frac{m_B - m_V}{2m_V}A_2^V(q^2), \tag{8}$$

$$A_0^V(0) = A_3^V(0), \tag{9}$$

$$\langle V|\partial_\mu A^\mu|B\rangle = 2m_V(\epsilon^* p_B)A_0^V(q^2), \tag{10}$$

where V represents a ρ or ω meson, and p, ϵ^* and m_V are the 4-momentum, polarization 4-vector and mass of the vector meson, respectively. Again, for light leptons (e and μ), the term proportional to q_μ is negligible so that, in effect, the decay rate depends only on the form factors $A_1(q^2)$, $A_2(q^2)$ and $V(q^2)$.

In the case $\bar{B} \to \rho\ell^-\bar{\nu}_\ell$ where the ρ meson decays into two pions $\rho \to \pi\pi$, the fully differential decay rate in the helicity basis is

$$\begin{aligned} \frac{\mathrm{d}\Gamma}{\mathrm{d}q^2\mathrm{d}\cos\theta_\ell\mathrm{d}\cos\theta_V\mathrm{d}\chi\mathrm{d}m_V} &= \frac{3}{8(4\pi)^4}G_F^2|V_{ub}|^2\frac{|\vec{p}_V|q^2}{m_B^2}|\mathrm{BW}(m_V)|^2[(1 - \eta\cos\theta_\ell)^2\sin^2\theta_V|H_+(q^2, m_V)|^2 \\ &\quad + (1 + \eta\cos\theta_\ell)^2\sin^2\theta_V|H_-(q^2, m_V)|^2 + 4\sin^2\theta_\ell\cos^2\theta_V|H_0(q^2, m_V)|^2 \\ &\quad - 4\eta\sin\theta_\ell\sin\theta_V\cos\theta_V\cos\chi H_0(q^2, m_V)((1 - \eta\cos\theta_\ell)H_+(q^2, m_V) \\ &\quad - (1 + \eta\cos\theta_\ell)H_-(q^2, m_V)) - 2\sin^2\theta_\ell\sin^2\theta_V\cos 2\chi H_+(q^2, m_V)H_-(q^2, m_V)], \end{aligned} \tag{11}$$

where $\mathrm{BW}(m_V)$ represents the resonance line shape, m_V is the invariant mass of the recoiling hadron, $|\vec{p}_V|$ is the magnitude of the vector meson momentum in the B meson rest frame, θ_ℓ is the polar angle of the lepton in the W boson rest frame with respect to the W flight direction in the B rest frame, θ_V is the polar angle of one of the pseudoscalar daughters in the rest frame of the vector meson with respect to the vector meson flight direction in the B rest frame, and χ is the angle between the decay planes of the W boson and the vector meson. The factor η is equal to $+1$ for semileptonic B-meson decays.

The differential decay rate for $B^- \to \omega\ell^-\bar{\nu}_\ell$, integrated over angular variables, is

$$\begin{aligned} \frac{\mathrm{d}\Gamma}{\mathrm{d}q^2\mathrm{d}m_V} &= \frac{1}{96\pi^3}G_F^2|V_{ub}|^2\frac{|\vec{p}_V|q^2}{m_B^2}|\mathrm{BW}(m_V)|^2 \\ &\quad \times[|H_0(q^2, m_V)|^2 + |H_+(q^2, m_V)|^2 \\ &\quad + |H_-(q^2, m_V)|^2]. \end{aligned} \tag{12}$$

In the above expressions, the helicity amplitudes are

$$\begin{aligned} H_\pm(q^2, m_V) &= (m_B + m_V)A_1^V(q^2) \mp \frac{2m_B|\vec{p}_V|}{m_B + m_V}V^V(q^2), \\ H_0(q^2, m_V) &= \frac{m_B + m_V}{2m_V\sqrt{q^2}}\left[(m_B^2 - m_V^2 - q^2)A_1^V(q^2)\right. \\ &\quad \left. - 4\frac{m_B^2|\vec{p}_V|^2}{(m_B + m_V)^2}A_2^V(q^2)\right]. \end{aligned} \tag{13}$$

For $\bar{B} \to \rho \ell^- \bar{\nu}_\ell$ decay, a relativistic Breit-Wigner function is used to describe the ρ line shape. The amplitude is

$$\mathrm{BW}(m_{\pi\pi}) = \frac{|\vec{p}_\pi|}{m_{\pi\pi}^2 - m_\rho^2 + i m_{\pi\pi} \Gamma(m_{\pi\pi})} \frac{B(|\vec{p}_\pi|)}{B(|\vec{p}'_\pi|)}, \quad (14)$$

where m_ρ is the nominal ρ mass, $|\vec{p}_\pi|$ is the pion momentum in the ρ rest frame, $|\vec{p}'_\pi|$ is the same but for fixed $m_{\pi\pi} = m_\rho$ and

$$\Gamma(m_{\pi\pi}) = \Gamma_0 \left(\frac{|\vec{p}_\pi|}{|\vec{p}'_\pi|}\right)^3 \frac{m_\rho}{m_{\pi\pi}} \left(\frac{B(|\vec{p}_\pi|)}{B(|\vec{p}'_\pi|)}\right)^2, \quad (15)$$

where Γ_0 is the nominal ρ width, and $B(x)$ is a Blatt-Weisskopf damping factor given by

$$B(x) = \frac{1}{\sqrt{1 + R^2 x^2}}, \quad (16)$$

with $R = 3\ (\mathrm{GeV}/c)^{-1}$.

For the $B^- \to \omega \ell^- \bar{\nu}_\ell$ decay, a simpler nonrelativistic form of the Breit-Wigner function is used for the ω line shape:

$$|\mathrm{BW}(m)|^2 = \frac{1}{2\pi} \frac{\Gamma}{(m - m_\omega)^2 + (\Gamma/2)^2}, \quad (17)$$

where m_ω and Γ are the nominal mass and width of the ω meson.

III. DATA SAMPLE AND SIMULATION

We use Belle data collected at the energy corresponding to the maximum of the $\Upsilon(4S)$ resonance (10.58 GeV in the center-of-mass frame), equivalent to an integrated luminosity of 711 fb^{-1}. Using $\mathcal{B}(\Upsilon(4S) \to B^0 \bar{B}^0) = 0.486 \pm 0.006$ and $\mathcal{B}(\Upsilon(4S) \to B^+ B^-) = 0.514 \pm 0.006$ [5], we can estimate the numbers of produced neutral and charged B-meson pairs, $N_{B^0\bar{B}^0} = (373 \pm 7) \times 10^6$ and $N_{B^+B^-} = (398 \pm 7) \times 10^6$. We also utilize a sample of 79 fb^{-1} collected below the $B\bar{B}$ threshold to study the contribution of the $e^+e^- \to q\bar{q}$ process, the so-called continuum, where q is a u, d, s, or c quark.

Monte Carlo (MC) samples of $e^+e^- \to \Upsilon(4S) \to B\bar{B}$ and continuum, equivalent to 5 times the integrated luminosity, are used to study the major backgrounds. The simulation accounts for changes in background conditions and beam collision parameters. Final state radiation (FSR) from charged particles is modeled using the PHOTOS package [22].

Dedicated MC samples are generated for charmless semileptonic decays, which are not present in the samples mentioned above. The total number of generated events for the signal MC is based on the number of $B\bar{B}$ pairs in data, scaled by a factor of 20 and assuming branching fractions of $\mathcal{B}(\bar{B}^0 \to X_u^+ \ell^- \bar{\nu}_\ell) = 1.709 \times 10^{-3}$ and $\mathcal{B}(B^- \to X_u^0 \ell^- \bar{\nu}_\ell) = 1.835 \times 10^{-3}$.

Signal samples with $\bar{B} \to \pi \ell^- \bar{\nu}_\ell$, $\bar{B} \to \rho \ell^- \bar{\nu}_\ell$ and $B^- \to \omega \ell^- \bar{\nu}_\ell$ decays are modeled using light cone sum rule (LCSR) form factor predictions [23,24]. Other decays to exclusive meson states are modeled using the updated quark model by Isgur-Scora-Grinstein-Wise (ISGW2) [25]. The inclusive component of charmless semileptonic decays is modeled to leading order α_s based on a prediction in the heavy-quark expansion (HQE) framework [26]. The fragmentation process of the resulting parton to the final hadron state is modeled using the PYTHIA6.2 package [27].

In the analysis, for the $\bar{B} \to \pi \ell^- \bar{\nu}_\ell$ decay modes, the signal MC events are reweighted to reproduce the best parametrization by Bourrely, Caprini and Lellouch (BCL), Eq. 39 in [28], because the extrapolation of the LCSR prediction from [23] is inadequate for the high q^2 region.

IV. EVENT SELECTION

Semileptonic B-meson decay candidates in events passing the full reconstruction procedure are selected. This procedure provides a NeuroBayes output variable o_{tag} that varies from zero to unity and tends to have larger values in cases where the fully reconstructed tagging candidate is a correctly reconstructed B meson. To suppress continuum events, the o_{tag} variable, combined with 18 modified Fox-Wolfram moment variables [29] in a neural net, is used to form a variable, $o_{\mathrm{tag}}^{\mathrm{cs}}$. Only high quality hadronic tag candidates with $\ln o_{\mathrm{tag}}^{\mathrm{cs}} > -6$ are selected. This corresponds to a rejection of candidates with a probability to be a B meson of less than 0.25%. An additional selection criterion is applied based on the beam-constrained mass $M_{\mathrm{bc}} = \sqrt{E_{\mathrm{beam}}^2/c^4 - (\sum_i \vec{p}_i/c)^2}$, where E_{beam} is the beam energy in the center-of-mass frame and the $\vec{p}_i$ are the 3-momenta of the detected particles that form the B-meson candidate in the same frame. The candidate must satisfy the condition $M_{\mathrm{bc}} > 5.27\ \mathrm{GeV}/c^2$.

It is possible to have several B candidates after full reconstruction. In this case, depending on the recoiling system of interest, we select the candidate with the highest probability assigned by the full reconstruction algorithm.

All charged particles are required to originate from the region near the interaction point (IP) of the electron and positron beams. With respect to a cylindrical system with origin at the IP, axis of symmetry z aligned opposite the positron beam direction and radial coordinate r, this region is defined as $|z_{\mathrm{PCA}}| < 2$ cm and $r_{\mathrm{PCA}} < 0.4$ cm, where z_{PCA} and r_{PCA} are the coordinates of the point of closest approach (PCA) of the reconstructed charged particle to the z axis. All other charged particles are ignored. After applying the above, we treat all selected charged particles as originating from B-meson decays.

Electron candidates are identified using the ratio of the energy detected in the ECL to the track momentum, the ECL shower shape, position matching between the track and ECL cluster, the energy loss in the CDC, and the response of the ACC [30]. Muons are identified based on their penetration range and transverse scattering in the

KLM detector [31]. In the momentum region relevant to this analysis, charged leptons are identified with an efficiency of about 90% while the probability to misidentify a pion as an electron (muon) is 0.25% (1.4%). Charged pion candidates are selected with an efficiency of 85% and a kaon misidentification probability of 19%, based on the responses of the CDC, ACC and TOF subdetectors.

To reject leptons from γ conversions in the detector material and from J/ψ and ψ' decays, $M_{\ell\ell}$, the invariant mass of all oppositely charged lepton ($\ell = e$ or μ) pairs, is checked and particles are vetoed if $M_{\ell\ell} < 0.1\ \mathrm{GeV}/c^2$, $3.00\ \mathrm{GeV}/c^2 < M_{\ell\ell} < 3.12\ \mathrm{GeV}/c^2$ or $3.60\ \mathrm{GeV}/c^2 < M_{\ell\ell} < 3.75\ \mathrm{GeV}/c^2$.

After a tag candidate has been selected, we look for a lepton amongst the rest of the reconstructed particles not already assigned to this tagging B meson. For $B^{\pm}$, only leptons with the correct charge are selected, whereas for B^0, because of mixing, both lepton charges—in other words, all flavors regardless of the reconstructed flavor of the neutral B-meson tag—are accepted. A chosen electron must have a momentum in the laboratory frame $|\vec{p}_e^{\,\mathrm{lab}}| > 300\ \mathrm{MeV}/c$, while a muon must satisfy $|\vec{p}_\mu^{\,\mathrm{lab}}| > 600\ \mathrm{MeV}/c$. These thresholds are chosen based on the known performance properties of the Belle particle identification algorithms. If several particles pass these requirements, the particle with the highest probability to be a lepton, as assigned by the reconstruction algorithm, is selected.

In the electron case, we consider all photons in the event that do not belong to the tag side; if a photon is found whose direction lies within a 3° cone around the electron direction, we add the photon 4-momentum to that of the electron and exclude the photon from further analysis. In cases where more than one photon is found, only the nearest photon is merged with the electron.

From the tag side, we derive the signal B-meson momentum 4-vector in the $\Upsilon(4S)$ rest frame using only the tag direction, by explicitly requiring the invariant mass to be the B-meson mass:

$$\begin{aligned} p_{B_{\mathrm{sig}}} &\equiv (E_{B_{\mathrm{sig}}}/c, \vec{p}_{B_{\mathrm{sig}}}) \\ &= c\left(\frac{m_{\Upsilon(4S)}}{2}, -\frac{\vec{p}_{B_{\mathrm{tag}}}}{|\vec{p}_{B_{\mathrm{tag}}}|}\sqrt{\left(\frac{m_{\Upsilon(4S)}}{2}\right)^2 - m_B^2}\right). \end{aligned} \tag{18}$$

We select photons that are not assigned to the tag side with energy in the laboratory frame of $E_\gamma > 50$ MeV. To form a π^0 candidate, we take all possible combinations of two photons; those with invariant mass in the range $|M_{\gamma\gamma} - m_{\pi^0}| < 15\ \mathrm{MeV}/c^2$ are selected as π^0 candidates. The selection is shown in Fig. 4(b).

We require the number of signal-side charged particles, i.e., charged particles that have not been assigned to the tagging B-meson candidate, to equal the number of charged particles expected for the particular decay mode under study.

To calculate the residual energy, E_{ECL}, in the electromagnetic calorimeter, we use photons that have not been assigned to either the signal or tag sides. The photons are boosted from the laboratory frame to the $\Upsilon(4S)$ rest frame and the energies are summed. For each decay mode, the selection criterion on the residual energy is optimized for maximal signal significance.

Combining the momentum 4-vectors of the selected hadron system and the lepton on the signal side, and denoting the so-constructed pseudoparticle Y, we have $p_Y = p_{\mathrm{hadrons}} + p_\ell$. We can then calculate the cosine of the angle between the direction of the signal-side B meson and the Y in the $\Upsilon(4S)$ frame:

$$\cos\theta_{BY} = \frac{2E_{B_{\mathrm{sig}}}E_Y/c^2 - m_B^2c^2 - m_Y^2c^2}{2|\vec{p}_{B_{\mathrm{sig}}}||\vec{p}_Y|}, \tag{19}$$

where m_Y is the invariant mass of the pseudoparticle. For signal decays, the condition $|\cos\theta_{BY}| < 1$ must be fulfilled. Allowing for resolution effects, we select events using the loose selection $|\cos\theta_{BY}| \leq 3$, keeping all correctly reconstructed events and suppressing a majority of the background. This choice provides us with enough background events to fix background shapes in the fit procedure described below.

Having reconstructed the momentum 4-vectors of the candidate signal B meson and pseudoparticle Y, we define the missing momentum 4-vector as

$$p_{\mathrm{miss}} \equiv (E_{\mathrm{miss}}/c, \vec{p}_{\mathrm{miss}}) = p_{B_{\mathrm{sig}}} - p_Y. \tag{20}$$

For a correctly reconstructed semileptonic decay, p_{miss} represents the momentum 4-vector of a single missing neutrino, with missing mass squared $M_{\mathrm{miss}}^2 \equiv p_{\mathrm{miss}}^2/c^2$ consistent with zero.

The missing energy is required to satisfy $E_{\mathrm{miss}} > 300$ MeV to avoid backgrounds where the B meson decays hadronically but a pion from this decay is misidentified as a muon.

For $B^- \to \pi^0\ell^-\bar{\nu}_\ell$ candidates, we select the π^0 that gives the smallest value of the magnitude of M_{miss}^2, defined in this case as $|p_{B_{\mathrm{sig}}} - p_\ell - p_{\pi^0}|^2$. The angle $\psi_{\gamma\gamma}^{\mathrm{lab}}$ between photons from the π^0 decay must satisfy $\cos\psi_{\gamma\gamma}^{\mathrm{lab}} > 0.25$, which mainly suppresses background where one photon candidate arises from activity in the backward endcap and the other from the forward endcap, forming a fake π^0. The residual energy is required to satisfy the condition $E_{\mathrm{ECL}} < 0.6$ GeV.

For $\bar{B}^0 \to \pi^+\ell^-\bar{\nu}_\ell$ candidates, we require that both charged particles be close to each other at the PCA: $|z_{\mathrm{PCA}}^{\ell} - z_{\mathrm{PCA}}^{\pi^+}| < 1$ mm. Because the pion and lepton originate from the same vertex, they should have matching z-coordinate values at the start of the track, in the vicinity of the IP. We require the residual energy to satisfy $E_{\mathrm{ECL}} < 1$ GeV. In the case of the charged lepton being a muon, we test the hypothesis that the selected pion is actually a muon from a J/ψ decay misidentified as a pion, and reject events where $|M_{\mu\pi} - m_{J/\psi}| < 20\ \mathrm{MeV}/c^2$, assuming the muon hypothesis for both particles.

For $B^- \to \rho^0 \ell^- \bar{\nu}_\ell$ candidates, we require all charged particles to originate from the same vertex, $|z^{\ell}_{\mathrm{PCA}} - z^{\pi^\pm}_{\mathrm{PCA}}| < 1$ mm and $|z^{\pi^+}_{\mathrm{PCA}} - z^{\pi^-}_{\mathrm{PCA}}| < 1$ mm. The residual energy must satisfy $E_{\mathrm{ECL}} < 0.7$ GeV. We select events where the invariant mass of the two pions is around the nominal ρ meson mass, requiring $|M_{\pi^+\pi^-} - m_\rho| < 2\Gamma_\rho$ where $m_\rho = 775.5\ \mathrm{MeV}/c^2$ and $\Gamma_\rho = 149.1\ \mathrm{MeV}/c^2$ are the nominal ρ mass and decay width, respectively.

For $\bar{B}^0 \to \rho^+ \ell^- \bar{\nu}_\ell$ candidates, we select the $\pi^+\pi^0$ pair with the largest energy $E_{\pi^+\pi^0}$ in the $\Upsilon(4S)$ rest frame. The residual energy must satisfy $E_{\mathrm{ECL}} < 0.7$ GeV. The angle between the photons must satisfy $\cos\psi^{\mathrm{lab}}_{\gamma\gamma} > 0.4$. The two charged particles must originate from the same vertex: $|z^{\ell}_{\mathrm{PCA}} - z^{\pi^+}_{\mathrm{PCA}}| < 1$ mm. We reject events where the invariant mass of the two particles, assuming the muon hypothesis, lies close to the J/ψ mass, i.e., with $|M_{\mu\pi} - m_{J/\psi}| < 20\ \mathrm{MeV}/c^2$. As for $B^- \to \rho^0 \ell^- \bar{\nu}_\ell$, we require $|M_{\pi^+\pi^0} - m_\rho| < 2\Gamma_\rho$.

For $B^- \to \omega \ell^- \bar{\nu}_\ell$ candidates where $\omega \to \pi^+\pi^-\pi^0$, we select the $\pi^+\pi^-\pi^0$ combination containing the π^0 that has the invariant mass closest to the nominal ω meson mass, and we require $-40\ \mathrm{MeV}/c^2 < M_{\pi^+\pi^-\pi^0} - m_\omega < 30\ \mathrm{MeV}/c^2$, where $m_\omega = 782.65\ \mathrm{MeV}/c^2$. The residual energy must satisfy $E_{\mathrm{ECL}} < 0.5$ GeV. The angle between the photons must satisfy $\cos\psi^{\mathrm{lab}}_{\gamma\gamma} > 0.25$. The charged particles must originate from the same vertex: $|z^{\ell}_{\mathrm{PCA}} - z^{\pi^\pm}_{\mathrm{PCA}}| < 1$ mm and $|z^{\pi^+}_{\mathrm{PCA}} - z^{\pi^-}_{\mathrm{PCA}}| < 1$ mm.

For $B^- \to \omega \ell^- \bar{\nu}_\ell$ candidates where $\omega \to \pi^0\gamma$, we consider $\pi^0\gamma$ pairs for which $-40\ \mathrm{MeV}/c^2 < M_{\pi^0\gamma} - m_\omega < 30\ \mathrm{MeV}/c^2$ and then select the pair that gives the smallest value of $M^2_{\mathrm{miss}} = |p_{B_{\mathrm{sig}}} - p_\ell - p_{\pi^0\gamma}|^2$. The residual energy must satisfy $E_{\mathrm{ECL}} < 0.5$ GeV. The angle between the photons from the π^0 decay must satisfy $\cos\psi^{\mathrm{lab}}_{\gamma\gamma} > 0.4$. The angle θ_γ between the photon from the ω decay in the ω rest frame and the ω direction in the laboratory frame must satisfy $|\cos\theta_\gamma| < 0.5$.

V. HADRONIC TAG CALIBRATION

In this analysis, we use charmed semileptonic B-meson decays to calibrate the tagging efficiency, due to their large and well-known branching fractions. We can predict the number of events $N(B \to \mathrm{hadrons}, \bar{B} \to X_c \ell^- \bar{\nu}_\ell)$, where one B meson is reconstructed by the full reconstruction algorithm in a B-meson hadronic decay mode and the other B meson is reconstructed in an exclusive charmed semileptonic mode. We define

$$\begin{aligned} N(B &\to \mathrm{hadrons}, \bar{B} \to X_c \ell^- \bar{\nu}_\ell) \\ &= N_{B\bar{B}} \times \mathcal{B}(B \to \mathrm{hadrons}) \times \mathcal{B}(\bar{B} \to X_c \ell^- \bar{\nu}_\ell) \\ &\quad \times \varepsilon^{\mathrm{rec}}(B \to \mathrm{hadrons}, \bar{B} \to X_c \ell^- \bar{\nu}_\ell), \end{aligned} \tag{21}$$

where $\varepsilon^{\mathrm{rec}}(B \to \mathrm{hadrons}, \bar{B} \to X_c \ell^- \bar{\nu}_\ell)$ is the reconstruction efficiency for the specific tag and signal modes. To correct for the specific hadronic tag modes, we factorize the efficiency

$$\begin{aligned} \varepsilon^{\mathrm{rec}}&(B \to \mathrm{hadrons}, \bar{B} \to X_c \ell^- \bar{\nu}_\ell) \\ &= \varepsilon^{\mathrm{rec}}(B \to \mathrm{hadrons}) \times \varepsilon^{\mathrm{rec}}(\bar{B} \to X_c \ell^- \bar{\nu}_\ell) \times C, \end{aligned} \tag{22}$$

where C is a correlation factor due to tag- and signal-side interference. We assume that the MC accurately describes the product $\varepsilon^{\mathrm{rec}}(\bar{B} \to X_c \ell^- \bar{\nu}_\ell) \times C$ because the dynamics of exclusive $\bar{B} \to X_c \ell^- \bar{\nu}_\ell$ decays are well known.

The decay rates in the MC used to calibrate the hadronic tag efficiency are reweighted to the recent Particle Data Group (PDG) values using the correction factors given in Table I. We adjust the number of produced $B^0\bar{B}^0$ and B^+B^- pairs in the MC, which were produced with the assumption of an equal production rate, using the $\Upsilon(4S)$ branching fractions into B mesons mentioned in Sec. III.

To evaluate the tag correction factor, we fit the M^2_{miss} distribution separately for each hadronic tag mode, split by the charmed semileptonic mode. For each tag mode, we calculate the average correction factor over all charmed semileptonic modes and use it to reweight events in the MC.

The effect of the tag efficiency correction evaluated with the applied selection criteria is shown in Table II for all charmless semileptonic decays studied. The statistical precision of the calibration is 1.3% for $B^\pm$ and 1.8% for B^0 decay modes. We estimate the systematic uncertainty due to the PDG branching fraction uncertainties to be 3.0% for $B^\pm$ and 2.5% for B^0 decay modes. To select semileptonic decays with $D^{(*)}$ mesons, we use the particle identification capabilities of the Belle detector. We estimate the systematic uncertainty due to particle identification for the B^+ tag

TABLE I. Branching fractions with uncertainties from PDG [5], used for the hadronic tag calibration, as well as the branching fraction used in the Belle MC.

Decay process	$\mathcal{B}^{\mathrm{PDG}}$, %	$\mathcal{B}^{\mathrm{MC}}$, %	$\mathcal{B}$ ratio
$B^- \to D^0 \ell^- \bar{\nu}_\ell$	2.23 ± 0.11	2.31	0.965
$B^- \to D^{*0} \ell^- \bar{\nu}_\ell$	5.68 ± 0.19	5.79	0.981
$\bar{B}^0 \to D^+ \ell^- \bar{\nu}_\ell$	2.17 ± 0.12	2.13	1.019
$\bar{B}^0 \to D^{*+} \ell^- \bar{\nu}_\ell$	5.05 ± 0.12	5.33	0.947
$D^0 \to K^-\pi^+$	3.87 ± 0.05	3.82	1.013
$D^0 \to K^-\pi^+\pi^0$	13.9 ± 0.5	13.43	1.035
$D^0 \to K^-2\pi^+\pi^-$	8.07 ± 0.20	7.155	1.128
$D^+ \to K^-2\pi^+$	9.13 ± 0.19	9.594	0.952
$D^+ \to K^-2\pi^+\pi^0$	5.99 ± 0.18	6.03	0.993
$D^+ \to K^-3\pi^+\pi^-$	0.56 ± 0.05	0.6252	0.896
$D^{*0} \to D^0\pi^0$	61.9 ± 2.9	61.9	1.000
$D^{*0} \to D^0\gamma$	38.1 ± 2.9	38.1	1.000
$D^{*+} \to D^0\pi^+$	67.7 ± 0.5	67.7	1.000
$D^{*+} \to D^+\pi^0$	30.7 ± 0.5	30.7	1.000

TABLE II. The number of selected signal events before ($N_{\rm MC}$) and after ($N_{\rm MC}^{\rm tagc}$) tag efficiency corrections in MC for the studied decays.

Tag mode	Decay process	$N_{\rm MC}$	$N_{\rm MC}^{\rm tagc}$	$N_{\rm MC}^{\rm tagc}/N_{\rm MC}$
B^0 tag	$\bar{B}^0 \to \pi^+\ell^-\bar{\nu}_\ell$	591.6	421.3	0.71
	$\bar{B}^0 \to \rho^+\ell^-\bar{\nu}_\ell$	397.0	295.1	0.74
$B^\pm$ tag	$B^- \to \pi^0\ell^-\bar{\nu}_\ell$	280.3	211.1	0.75
	$B^- \to \rho^0\ell^-\bar{\nu}_\ell$	634.9	505.1	0.80
	$B^- \to \omega(3\pi)\ell^-\bar{\nu}_\ell$	129.0	104.1	0.81
	$B^- \to \omega(\pi^0\gamma)\ell^-\bar{\nu}_\ell$	12.1	9.8	0.81

to be 2.3% and for the B^0 tag 3.0%. The total uncertainty of the tag correction, with correlations between modes included, is estimated to be 4.2% for B^+ and 4.5% for B^0. We do not count the lepton identification correction and its uncertainty as part of the systematic uncertainty because it cancels in the ratio for the studied charmless semileptonic decays.

VI. SIGNAL EXTRACTION

To obtain the number of signal events passing all selection criteria for any given decay mode, we fit the $M^2_{\rm miss}$ distribution, for which signal events are expected to peak at $M^2_{\rm miss} = 0$. We use a maximum likelihood technique [32] which also takes into account finite MC statistics in the template histograms that form the components of the fit. The effect on the fitting procedure of using MC $M^2_{\rm miss}$ templates with finite statistics is checked using a toy MC procedure. We find that the fit procedure itself does not introduce a bias for the decay modes studied, and parameter uncertainties match expectations.

A. Components of the fit

To describe the data $M^2_{\rm miss}$ distributions, we divide the MC samples into various components, each defining a template, depending on the decay mode studied. To better describe the amount of $\bar{B} \to X_u\ell^-\bar{\nu}_\ell$ cross-feed, we adjust, where relevant, the MC branching fractions to those obtained in this study.

For the $B^- \to \pi^0\ell^-\bar{\nu}_\ell$ decay, we define the following components: $B^- \to \pi^0\ell^-\bar{\nu}_\ell$ signal, $\bar{B} \to X_u\ell^-\bar{\nu}_\ell$ cross-feed, other B-meson decays and $q\bar{q}$ continuum. The continuum component is fixed to the MC prediction, and the normalizations of all other components are free parameters of the fit.

For the $\bar{B}^0 \to \pi^+\ell^-\bar{\nu}_\ell$ decay, we define the following components: $\bar{B}^0 \to \pi^+\ell^-\bar{\nu}_\ell$ signal, $\bar{B}^0 \to \rho^+\ell^-\bar{\nu}_\ell$ cross-feed, other $\bar{B} \to X_u\ell^-\bar{\nu}_\ell$ cross-feed, other B-meson decays and $q\bar{q}$ continuum. The continuum component is fixed to the MC prediction, the amount of $\bar{B}^0 \to \rho^+\ell^-\bar{\nu}_\ell$ cross-feed is fixed to the value obtained in the $\bar{B}^0 \to \rho^+\ell^-\bar{\nu}_\ell$ fit, and all other components are free parameters of the fit.

For the $B^- \to \rho^0\ell^-\bar{\nu}_\ell$ decay, we define the following components: $B^- \to \rho^0\ell^-\bar{\nu}_\ell$ signal, $B^- \to f_0(980)\ell^-\bar{\nu}_\ell$, $B^- \to f_2(1270)\ell^-\bar{\nu}_\ell$, $B^- \to \omega\ell^-\bar{\nu}_\ell$, other $\bar{B} \to X_u\ell^-\bar{\nu}_\ell$ cross-feed, $B^- \to D^{(*)0}\ell^-\bar{\nu}_\ell$ in which the D^0 decays to $K^-\pi^+$ or $\pi^+\pi^-$ final states, other B-meson decays and $q\bar{q}$ continuum. The continuum, $B^- \to f_0(980)\ell^-\bar{\nu}_\ell$ and $B^- \to \omega\ell^-\bar{\nu}_\ell$ components are small and fixed to the MC prediction; the amounts of $B^- \to f_2(1270)\ell^-\bar{\nu}_\ell$, $B^- \to D^{(*)0}\ell^-\bar{\nu}_\ell$ in which the D^0 decays to $K^-\pi^+$ or $\pi^+\pi^-$ final states and cross-feeds are fixed to the values obtained from the invariant mass fit that is described later. All other components are free parameters of the fit.

For the $\bar{B}^0 \to \rho^+\ell^-\bar{\nu}_\ell$ decay, we define the following components: $\bar{B}^0 \to \rho^+\ell^-\bar{\nu}_\ell$ signal, $\bar{B}^0 \to \pi^+\ell^-\bar{\nu}_\ell$ cross-feed, other $\bar{B} \to X_u\ell^-\bar{\nu}_\ell$ cross-feed, $\bar{B}^0 \to D^{(*)+}\ell^-\bar{\nu}_\ell$ in which the D^+ decays to $\pi^+\pi^0$, other B-meson decays and $q\bar{q}$ continuum. The continuum component is fixed to the MC prediction, the amount of $\bar{B}^0 \to \pi^+\ell^-\bar{\nu}_\ell$ cross-feed is fixed to the values obtained in the $\bar{B}^0 \to \pi^+\ell^-\bar{\nu}_\ell$ fit, and the amount of $\bar{B}^0 \to D^{(*)+}\ell^-\bar{\nu}_\ell$ in which the D^+ decays to $\pi^+\pi^0$ is fixed to the value obtained from the invariant mass fit. The normalizations of all other components are free parameters of the fit.

For the $B^- \to \omega\ell^-\bar{\nu}_\ell$ decay, we define the following components: $B^- \to \omega\ell^-\bar{\nu}_\ell$ signal ($\omega \to \pi^+\pi^-\pi^0$ or $\omega \to \pi^0\gamma$), $\bar{B} \to X_u\ell^-\bar{\nu}_\ell$ cross-feed, other B-meson decays and $q\bar{q}$ continuum. The continuum component is fixed to the MC prediction, and all other components are free parameters of the fit.

B. Fit results

The fitted $M^2_{\rm miss}$ distributions are shown in Fig. 1 for $\bar{B} \to \pi\ell^-\bar{\nu}_\ell$ decays, in Fig. 2 for $\bar{B} \to \rho\ell^-\bar{\nu}_\ell$ decays and in Fig. 3 for $B^- \to \omega\ell^-\bar{\nu}_\ell$ decays.

The parameter values obtained from the fit, as well as the values of the fixed parameters, are presented in Tables III, IV, V, VI, and VII.

Figure 4 shows various kinematic variables as well as the selection criteria for several decay modes. In these figures, the MC components have been scaled according to the fit result. The same distributions for other decay modes also show similar levels of data/MC agreement and are not shown here.

Since the signal MC has been generated in proportion to the number of $B\bar{B}$ pairs, the assumption of efficiency cancellation lets us evaluate the branching fraction of specific semileptonic decay modes over the entire B meson decay phase space as follows:

$$\mathcal{B}^{\rm DATA}(B \to X_u\ell\nu) = \mathcal{B}^{\rm MC}(B \to X_u\ell\nu)\frac{N^{\rm fit}}{N^{\rm MC}}, \qquad (23)$$

where $N^{\rm fit}$ is the fitted signal yield, and $N^{\rm MC}$ is the number of signal events in MC with efficiency corrections applied. The fitted signal yields and corresponding MC predictions, along with the resulting branching fractions,

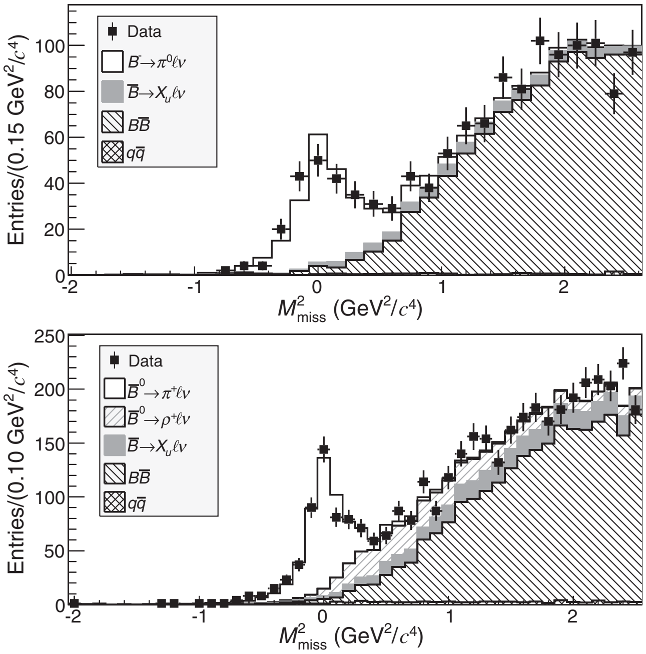

FIG. 1. Fit to the M^2_{miss} distributions in data for $B^- \to \pi^0 \ell^- \bar{\nu}_\ell$ decays (top) and $\bar{B}^0 \to \pi^+ \ell^- \bar{\nu}_\ell$ decays (bottom). The fit components are described in the text.

are summarized in Table VIII. Because of the marginal contribution of the $B^- \to \omega(\pi^0 \gamma)\ell^- \bar{\nu}_\ell$ decay, as seen in this table, we do not consider this mode further. The systematic uncertainties are described below.

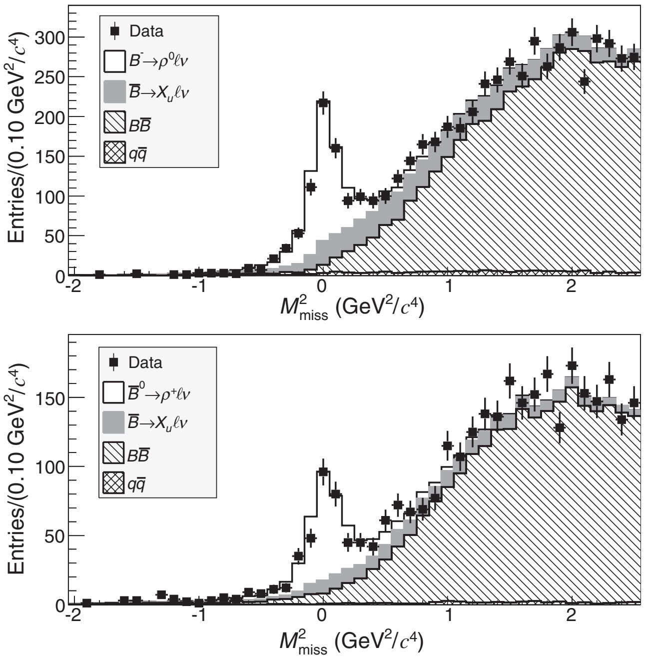

FIG. 2. Fit to the M^2_{miss} distribution in data for $B^- \to \rho^0 \ell^- \bar{\nu}_\ell$ decays (top) and $\bar{B}^0 \to \rho^+ \ell^- \bar{\nu}_\ell$ (bottom). The fit components are described in the text.

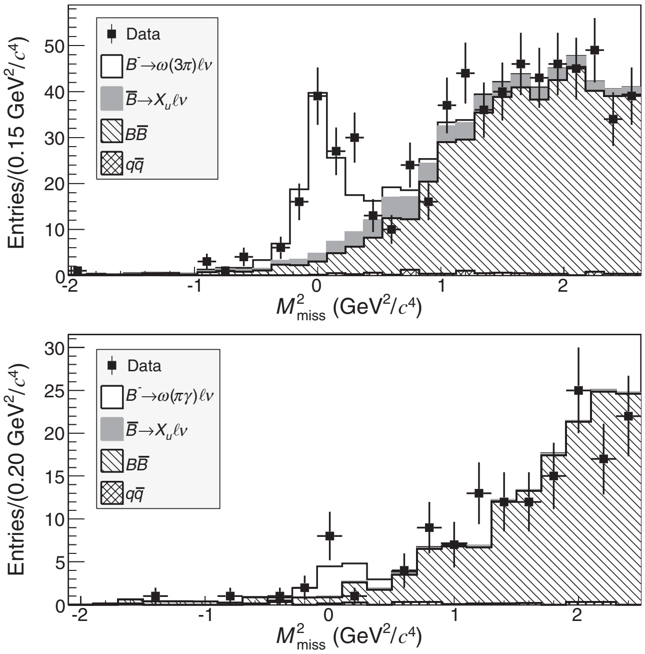

FIG. 3. Fit to the M^2_{miss} distribution in data for $B^- \to \omega \ell^- \bar{\nu}_\ell$ decays where $\omega \to \pi^+ \pi^- \pi^0$ (top) and $\omega \to \pi^0 \gamma$ (bottom). The fit components are described in the text.

C. Signal extraction in bins of q^2

We also perform signal extractions in bins of q^2. To obtain the number of signal events, we perform a two-dimensional binned maximum likelihood fit in the q^2-M^2_{miss} plane. The shapes of the fit components are taken from MC, and they are organized as described above. The signal component, as well as the $B\bar{B}$ component, is allowed to float in each q^2 bin independently. The rest of the

TABLE III. Fitted yields for $B^- \to \pi^0 \ell^- \bar{\nu}_\ell$ decays.

Component	Yield
$B^- \to \pi^0 \ell^- \bar{\nu}_\ell$	232.2 ± 22.6
$\bar{B} \to X_u \ell^- \bar{\nu}_\ell$	100.0 ± 86.7
$B\bar{B}$	1993.4 ± 90.7
$q\bar{q}$	18.5(fixed)
χ^2/ndf	56.3/50

TABLE IV. Fitted yields for $\bar{B}^0 \to \pi^+ \ell^- \bar{\nu}_\ell$ decays.

Component	Yield
$\bar{B}^0 \to \pi^+ \ell^- \bar{\nu}_\ell$	462.6 ± 27.7
$\bar{B}^0 \to \rho^+ \ell^- \bar{\nu}_\ell$	514.5(fixed)
$\bar{B} \to X_u \ell^- \bar{\nu}_\ell$	599.5 ± 198.4
$B\bar{B}$	5511.6 ± 200.7
$q\bar{q}$	111.8(fixed)
χ^2/ndf	76.0/76

TABLE V. Fitted yields for $B^- \to \rho^0 \ell^- \bar{\nu}_\ell$ decays.

Component	Yield
$B^- \to \rho^0 \ell^- \bar{\nu}_\ell$	621.7 ± 35.0
$\bar{B} \to X_u \ell^- \bar{\nu}_\ell$	757.3 ± 109.0
$B\bar{B}$	6901.6 ± 128.9
$B^- \to f_2(1270)\ell^- \bar{\nu}_\ell$	13.3(fixed)
$B^- \to D^{(*)0}(K^- \pi^+)\ell^- \bar{\nu}_\ell$	25.1(fixed)
$B^- \to D^{(*)0}(\pi^+ \pi^-)\ell^- \bar{\nu}_\ell$	1.2(fixed)
$B^- \to \omega(\pi\pi)\ell^- \bar{\nu}_\ell$	6.1(fixed)
$B^- \to f_0(980)\ell^- \bar{\nu}_\ell$	9.5(fixed)
$q\bar{q}$	169.9(fixed)
χ^2/ndf	59.5/52

TABLE VI. Fitted yields for $\bar{B}^0 \to \rho^+ \ell^- \bar{\nu}_\ell$ decays.

Component	Yield
$\bar{B}^0 \to \rho^+ \ell^- \bar{\nu}_\ell$	343.3 ± 28.3
$\bar{B} \to X_u \ell^- \bar{\nu}_\ell$	243.4 ± 91.6
$B\bar{B}$	4039.7 ± 105.1
$q\bar{q}$	59.2(fixed)
$\bar{B}^0 \to \pi^+ \ell^- \bar{\nu}_\ell$	10.5(fixed)
$\bar{B}^0 \to D^{(*)+}(\pi^+ \pi^0)\ell^- \bar{\nu}_\ell$	1.3(fixed)
χ^2/ndf	84.4/65

TABLE VII. Fitted yields for $B^- \to \omega \ell^- \bar{\nu}_\ell$ decays.

	Yield	
Component	$\omega \to \pi^+ \pi^- \pi^0$	$\omega \to \pi^0 \gamma$
$B^- \to \omega \ell^- \bar{\nu}_\ell$	96.7 ± 14.5	9.0 ± 4.0
$\bar{B} \to X_u \ell^- \bar{\nu}_\ell$	62.3 ± 38.0	2.2 ± 11.4
$B\bar{B}$	763.6 ± 43.2	287.4 ± 19.0
$q\bar{q}$	10.8 (fixed)	4.4 (fixed)
χ^2/ndf	55.8/43	41.4/32

components are varied or fixed in the same manner as in the q^2-independent M^2_{miss} fit, and the parameters of the fit are the yields of each component in the entire q^2-M^2_{miss} plane. The M^2_{miss} distributions are shown in Fig. 5 for $B^- \to \pi^0 \ell^- \bar{\nu}_\ell$ decays, Fig. 6 for $\bar{B}^0 \to \pi^+ \ell^- \bar{\nu}_\ell$ decays, Fig. 7 for $B^- \to \rho^0 \ell^- \bar{\nu}_\ell$ decays, Fig. 8 for $\bar{B}^0 \to \rho^+ \ell^- \bar{\nu}_\ell$ decays and Fig. 9 for $B^- \to \omega(3\pi)\ell^- \bar{\nu}_\ell$ decays. We correct for the effects of finite detector resolution and bremsstrahlung on the q^2 distributions using a simple unfolding procedure described in our previous untagged measurement [13]. The extracted yields and partial branching fractions, as well as the full statistical correlation matrices, are given in the Appendix. A comparison of the yields and resulting branching fractions obtained from the fits in bins of q^2 with those obtained from fits to the entire q^2 range is shown in Table IX. As can be seen, they are in excellent agreement.

D. Discussion

In the case of exact isospin symmetry, there are known relations between hadronic states with different isospin projections. For $\bar{B} \to \pi \ell^- \bar{\nu}_\ell$ decays,

$$2 \times \frac{\mathcal{B}(B^- \to \pi^0 \ell^- \bar{\nu}_\ell)}{\mathcal{B}(\bar{B}^0 \to \pi^+ \ell^- \bar{\nu}_\ell)} \frac{\tau_{B^0}}{\tau_{B^+}} = 1 \tag{24}$$

and similarly, for $\bar{B} \to \rho \ell^- \bar{\nu}_\ell$ decays,

$$2 \times \frac{\mathcal{B}(B^- \to \rho^0 \ell^- \bar{\nu}_\ell)}{\mathcal{B}(\bar{B}^0 \to \rho^+ \ell^- \bar{\nu}_\ell)} \frac{\tau_{B^0}}{\tau_{B^+}} = 1. \tag{25}$$

Using the lifetime ratio of neutral to charged B mesons from the PDG [5], $\tau_{B^+}/\tau_{B^0} = 1.079 \pm 0.007$, we can test the isospin relations using the obtained branching fractions and taking into account correlations between measurements:

$$\begin{aligned} 2 \times \frac{\mathcal{B}(B^- \to \pi^0 \ell^- \bar{\nu}_\ell)}{\mathcal{B}(\bar{B}^0 \to \pi^+ \ell^- \bar{\nu}_\ell)} \frac{\tau_{B^0}}{\tau_{B^+}} \\ = 0.997 \pm 0.114_{\mathrm{stat}} \pm 0.053_{\mathrm{syst}} \approx 1.00 \pm 0.13_{\mathrm{tot}} \end{aligned} \tag{26}$$

and

$$\begin{aligned} 2 \times \frac{\mathcal{B}(B^- \to \rho^0 \ell^- \bar{\nu}_\ell)}{\mathcal{B}(\bar{B}^0 \to \rho^+ \ell^- \bar{\nu}_\ell)} \frac{\tau_{B^0}}{\tau_{B^+}} \\ = 1.055 \pm 0.105_{\mathrm{stat}} \pm 0.081_{\mathrm{syst}} \approx 1.06 \pm 0.13_{\mathrm{tot}}, \end{aligned} \tag{27}$$

which are in good agreement with the predictions. Using isospin relations, we can present results for the combined branching fractions, taking into account correlations in the systematic uncertainties:

$$\begin{aligned} \mathcal{B}(\bar{B}^0 \to \pi^+ \ell^- \bar{\nu}_\ell) &= (1.49 \pm 0.08_{\mathrm{stat}} \pm 0.07_{\mathrm{syst}}) \times 10^{-4} \\ &= (1.49 \pm 0.10_{\mathrm{tot}}) \times 10^{-4} \end{aligned} \tag{28}$$

and

$$\begin{aligned} \mathcal{B}(\bar{B}^0 \to \rho^+ \ell^- \bar{\nu}_\ell) &= (3.34 \pm 0.16_{\mathrm{stat}} \pm 0.17_{\mathrm{syst}}) \times 10^{-4} \\ &= (3.34 \pm 0.23_{\mathrm{tot}}) \times 10^{-4}, \end{aligned} \tag{29}$$

where the total error is obtained by adding the statistical and systematic uncertainties in quadrature. For $\bar{B} \to \pi \ell^- \bar{\nu}_\ell$ decay, this measurement agrees with recent untagged results from Belle [13] and *BABAR* [12] at a similar level of precision. For $\bar{B} \to \rho \ell^- \bar{\nu}_\ell$ decay, the branching fraction is 43% (2.7σ) higher than the current PDG value $\mathcal{B}^{\mathrm{PDG}}(\bar{B} \to \rho \ell^- \bar{\nu}_\ell) = (2.34 \pm 0.15 \pm 0.24) \times 10^{-4}$ and the precision is almost twice that of the PDG value.

The branching fraction of $B^- \to \omega \ell^- \bar{\nu}_\ell$ decay is in good agreement with the PDG value $\mathcal{B}^{\mathrm{PDG}}(B^- \to \omega \ell^- \bar{\nu}_\ell) = (1.15 \pm 0.17) \times 10^{-4}$ and has the same precision.

We note that the obtained branching fractions are fully inclusive of soft photon emission. As an example, the dependence of the reconstruction efficiency of the $\bar{B}^0 \to \pi^+ \ell^- \bar{\nu}_\ell$ decay on the energy carried away by photons is shown in Fig. 10. It is seen that the detection efficiency is

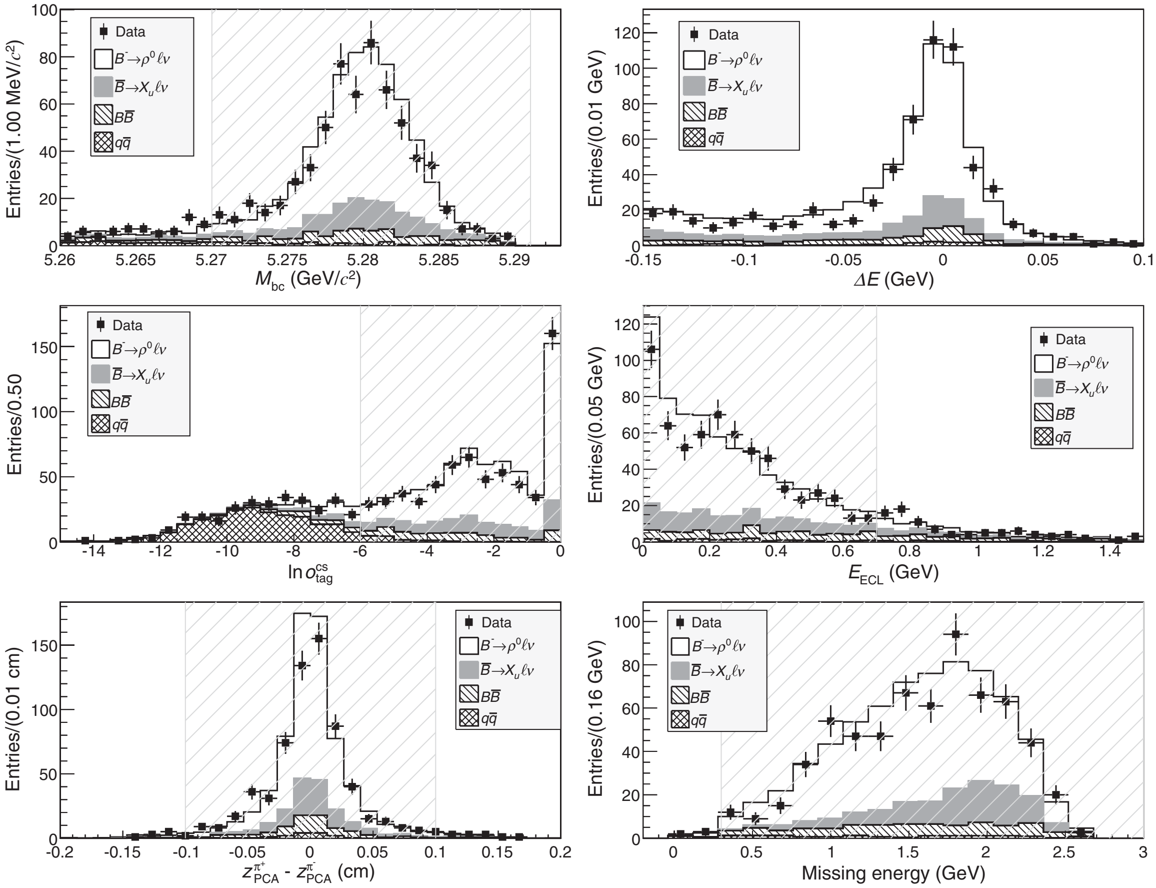

(a)Various kinematic variables for the $B^- \to \rho^0 \ell^- \bar{\nu}_\ell$ decay in the region $|M^2_{miss}| < 0.25$ GeV/c^2.

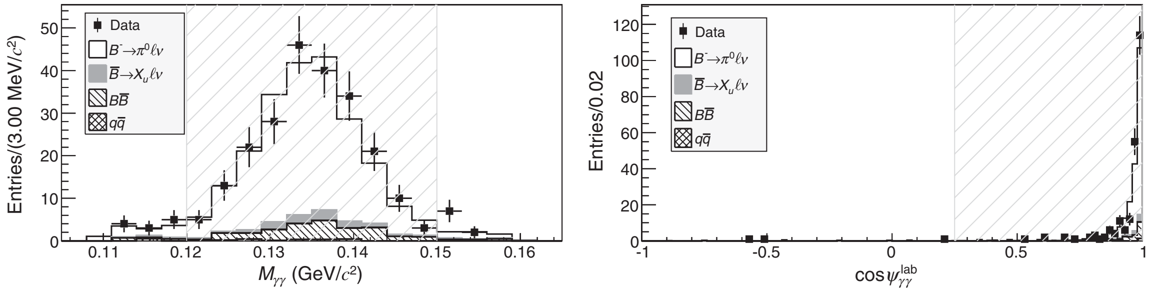

(b)Invariant mass of two photons and angles between two photons for the $B^- \to \pi^0 \ell^- \bar{\nu}_\ell$ decay in the region $|M^2_{miss}| < 0.5$ GeV/c^2.

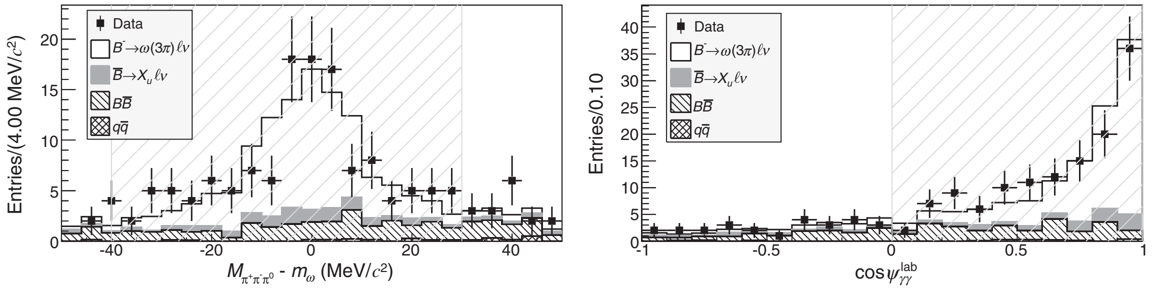

(c)Invariant mass of three pions and angle between photons from the π^0 decay for the $B^- \to \omega \ell^- \bar{\nu}_\ell$ decay in the region $|M^2_{miss}| < 0.5$ GeV/c^2.

FIG. 4. Data/MC comparison for (a) $B^- \to \rho^0 \ell^- \bar{\nu}_\ell$, (b) $B^- \to \pi^0 \ell^- \bar{\nu}_\ell$ and (c) $B^- \to \omega \ell^- \bar{\nu}_\ell$ decays, where corresponding components are scaled according to the result of the fit to the M^2_{miss} distribution. Where present, the hatched region shows the selection criterion on the corresponding variable. In each case M^2_{miss} is required to be close to zero, and all other selection criteria are applied except the one on the variable plotted.

TABLE VIII. The fitted yields and MC predictions, MC and resulting branching fractions in units of 10^{-4}. The experimental branching fractions are shown with both statistical (first) and experimental systematic uncertainties (second).

X_u	N^{fit}	N^{MC}	$\mathcal{B}^{\text{MC}}$	$\mathcal{B}^{\text{DATA}}$
π^0	232.2 ± 22.6	211.1	0.73	$0.80 \pm 0.08 \pm 0.04$
π^+	462.6 ± 27.7	421.3	1.36	$1.49 \pm 0.09 \pm 0.07$
ρ^0	621.7 ± 35.0	505.1	1.49	$1.83 \pm 0.10 \pm 0.10$
ρ^+	343.3 ± 28.3	295.1	2.77	$3.22 \pm 0.27 \pm 0.24$
$\omega(3\pi)$	96.7 ± 14.5	104.1	1.15	$1.07 \pm 0.16 \pm 0.07$
$\omega(\pi^0\gamma)$	9.0 ± 4.0	9.8	1.15	$1.06 \pm 0.47 \pm 0.07$
ω(average)			1.15	$1.07 \pm 0.15 \pm 0.07$

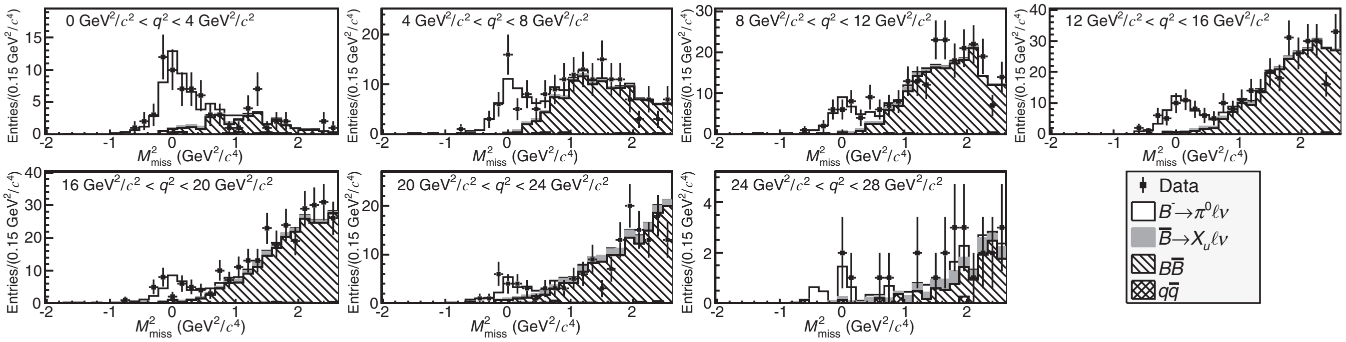

FIG. 5. Projection onto the M^2_{miss} axis of the fitted distribution to data for $B^- \to \pi^0 \ell^- \bar{\nu}_\ell$ decay, for 7 bins in q^2.

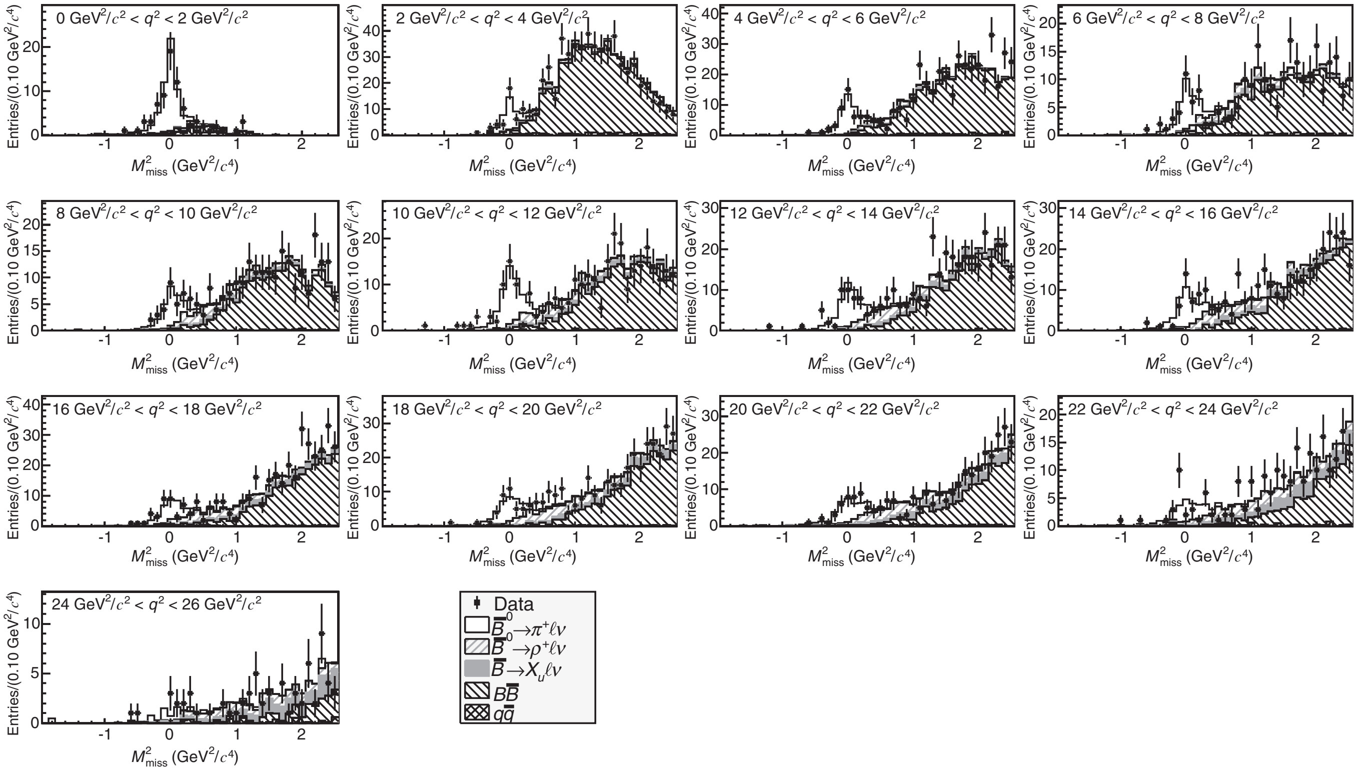

FIG. 6. Projection onto the M^2_{miss} axis of the fitted distribution to data for $\bar{B}^0 \to \pi^+ \ell^- \bar{\nu}_\ell$ decay, for 13 bins in q^2.

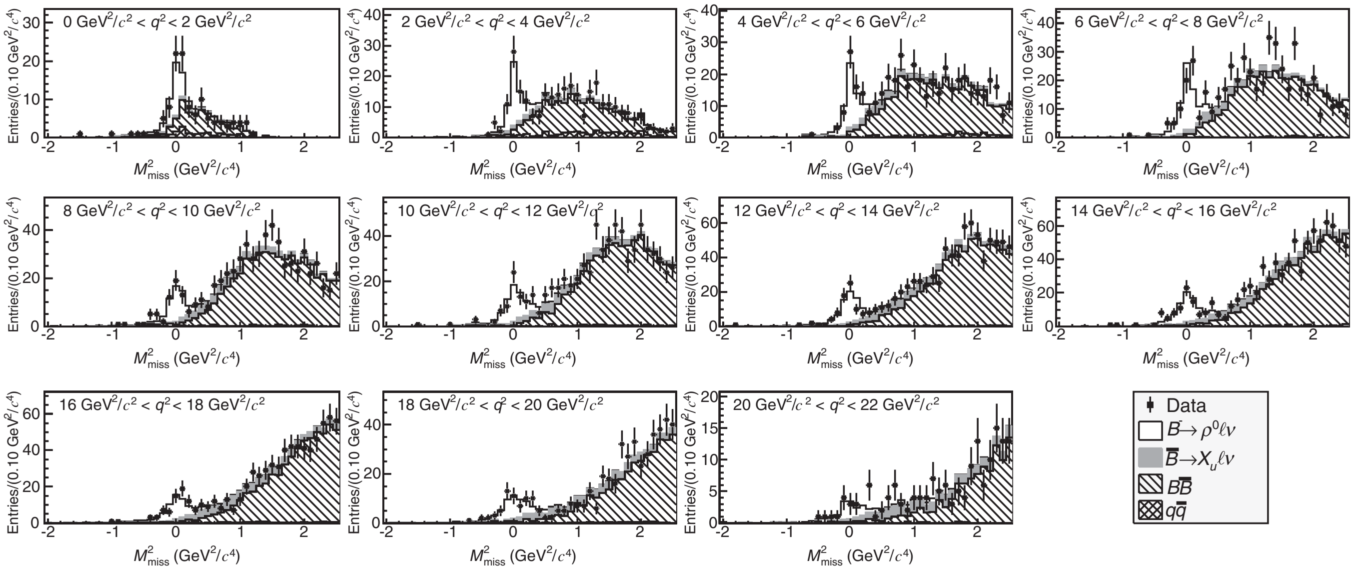

FIG. 7. Projection onto the M^2_{miss} axis of the fitted distribution to data for $B^- \to \rho^0 \ell^- \bar{\nu}_\ell$ decay, for 11 bins in q^2.

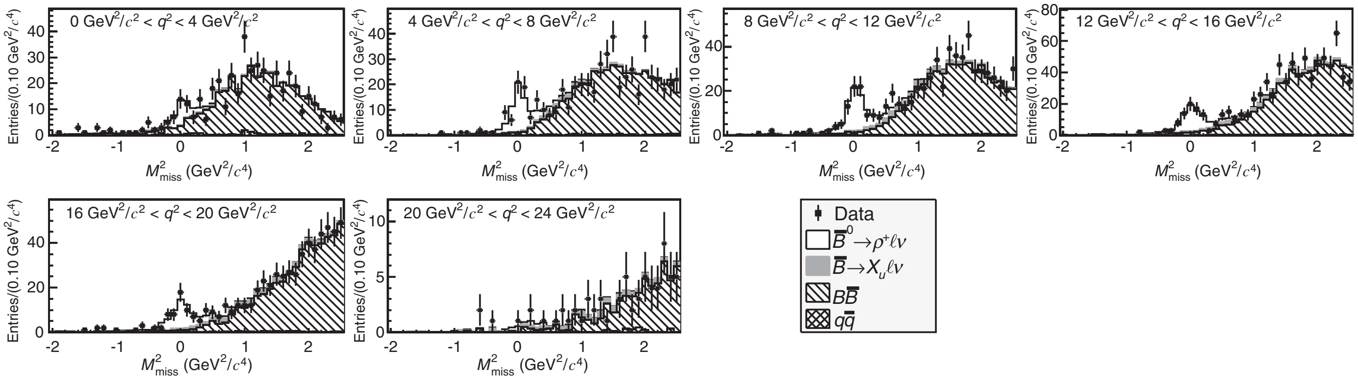

FIG. 8. Projection onto the M^2_{miss} axis of the fitted distribution to data for $\bar{B}^0 \to \rho^+ \ell^- \bar{\nu}_\ell$ decay, for 6 bins in q^2.

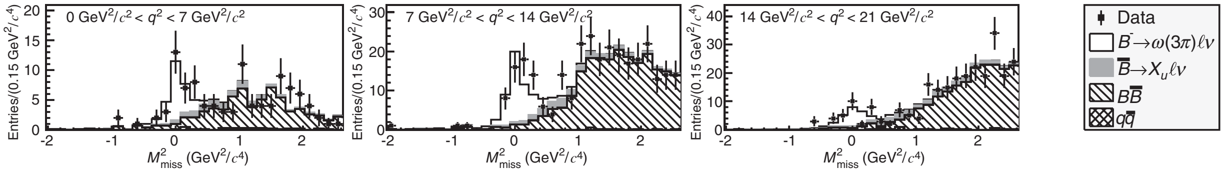

FIG. 9. Projection onto the M^2_{miss} axis of the fitted distribution to data for $B^- \to \omega \ell^- \bar{\nu}_\ell$ decay, for 3 bins in q^2.

TABLE IX. Comparison of signal yields and resulting branching fractions for the full q^2 range, obtained by summing over q^2 bins. Here ε is the total efficiency for the entire q^2 range.

X_u	N	$\sum \Delta N$	ε, 10^{-3}	$\mathcal{B}$, 10^{-4}	$\sum \Delta\mathcal{B}$, 10^{-4}
π^0	232.2 ± 22.6	233.3 ± 20.6	1.83 ± 0.03	0.80 ± 0.08 ± 0.04	0.81 ± 0.07 ± 0.04
π^+	462.6 ± 27.7	461.1 ± 27.4	2.07 ± 0.02	1.49 ± 0.09 ± 0.07	1.49 ± 0.09 ± 0.07
ρ^0	621.7 ± 35.0	621.9 ± 34.8	2.13 ± 0.02	1.83 ± 0.10 ± 0.10	1.84 ± 0.10 ± 0.10
ρ^+	343.3 ± 28.3	350.2 ± 27.3	0.72 ± 0.01	3.22 ± 0.27 ± 0.24	3.26 ± 0.26 ± 0.24
ω	96.7 ± 14.5	99.0 ± 15.0	0.64 ± 0.01	1.07 ± 0.16 ± 0.07	1.13 ± 0.18 ± 0.07

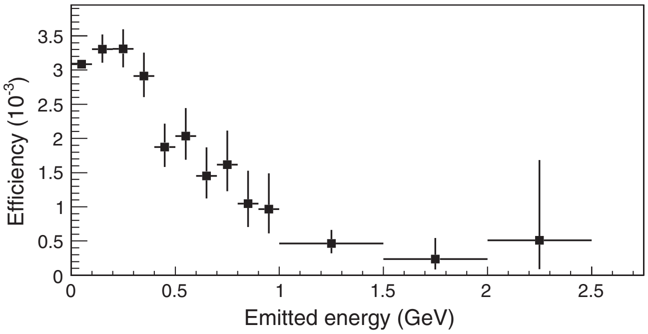

FIG. 10. Detection efficiency for $\bar{B}^0 \to \pi^+\ell^-\bar{\nu}_\ell$ decay as a function of the total emitted energy carried by photons.

constant for total emitted energy below 300 MeV, where the internal bremsstrahlung process should dominate; MC describes this process using the PHOTOS package. For higher emitted energies, the efficiency drops and should naturally suppress possible direct (or structure-dependent) emission, which is not included in MC.

VII. SYSTEMATIC UNCERTAINTIES

The systematic uncertainties are organized into two categories: those related to detector simulation, such as the charged track reconstruction efficiency, particle identification and neutral cluster reconstruction; and effects of the form factor model used in the MC.

The difference between the track reconstruction efficiency for data and MC is estimated using partially reconstructed D^* mesons and is found to be 0.35% per charged particle track. This difference is assigned as the track reconstruction systematic error.

We estimate the π^0 reconstruction efficiency uncertainty to be 2%, from a dedicated study of η decays in the modes $\eta \to \pi^+\pi^-\pi^0$ and $\eta \to \gamma\gamma$.

By evaluating the full reconstruction tag efficiency using charmed semileptonic decays of B mesons, we effectively measure the ratio of the branching fractions between charmed and charmless semileptonic decays. In this case, the systematic uncertainty due to the lepton identification mostly cancels. However, the momentum spectra of charmed and charmless semileptonic decays are not the same, and this leads to a small difference in the lepton identification efficiency, which we assign as a systematic uncertainty. We conservatively estimate this uncertainty to be the difference between the efficiencies for charmed and charmless semileptonic decay modes, and the value is 1%.

The K/π separation uncertainty appears in the analysis when we apply a kaon track veto. To obtain the effect of the kaon veto for each decay, the pion angular and momentum distributions are convoluted with the efficiency obtained from a dedicated study of particle identification efficiency using D^* decays. We estimate the uncertainty from the kaon veto to be ~1% per pion track.

We estimate the uncertainty from a possible shape variation in the M^2_{miss} template histogram for the $B\bar{B}$ component, due to inaccuracies in the charmed semileptonic decay branching fractions used in the MC, by varying these fractions according to the PDG values [5]. The variation in the extracted yields is $\leq 0.1\%$. Due to the smallness of this variation, this uncertainty is not listed in the summary systematic table.

We also establish that our branching fraction results are not sensitive to the particular values chosen for variables used in our selection criteria by varying these within reasonable limits and comparing the results obtained. We find that the variations in the extracted branching fractions stay within statistical fluctuations.

We assign a systematic uncertainty for the modeling of charmless semileptonic cross-feed for the $\bar{B}^0 \to \pi^+\ell^-\bar{\nu}_\ell$ decay and $\bar{B} \to \rho\ell^-\bar{\nu}_\ell$ decays where it was fixed in the fit procedure.

A. Background to the $\bar{B} \to \rho\ell^-\bar{\nu}_\ell$ decay

In the MC simulation, the inclusive component of charmless semileptonic B meson decays is generated using a HQE model, producing partons that are subsequently hadronized into various hadronic final states using the PYTHIA6.2 package [27]. The most difficult background for $\bar{B} \to \rho\ell^-\bar{\nu}_\ell$ is $\bar{B} \to X_u(\pi\pi)\ell^-\bar{\nu}_\ell$ with a nonresonant pion pair, because it is completely indistinguishable from signal when looking at the M^2_{miss} distribution alone.

To estimate the possible $\bar{B} \to X_u(\pi\pi)\ell^-\bar{\nu}_\ell$ nonresonant component, we perform a binned two-dimensional maximum likelihood fit to the $M_{\pi\pi}$-M^2_{miss} distribution both for $B^- \to \rho^0\ell^-\bar{\nu}_\ell$ and $\bar{B}^0 \to \rho^+\ell^-\bar{\nu}_\ell$ decays, where the bin size in M^2_{miss} is the same as shown in Fig. 2 and the bins in invariant mass are shown as vertical lines in Fig. 11. Additionally, this fit allows us to fix the yield of the $B^- \to f_2(1270)\ell^-\bar{\nu}_\ell$ decay where $f_2 \to \pi^+\pi^-$, and $B^- \to D^{(*)0}\ell^-\bar{\nu}_\ell$ where $D^0 \to K^+\pi^-$ and the kaon was misidentified as a pion, as well as $D^0 \to \pi^+\pi^-$. The $M_{\pi\pi}$ projections of the fitted distributions in the region $|M^2_{\mathrm{miss}}| < 0.25\ \mathrm{GeV}/c^2$, with the $\bar{B} \to X_u(\pi\pi)\ell^-\bar{\nu}_\ell$ component fixed to zero, are shown in Fig. 11. For illustration purposes, the yield of $\bar{B} \to X_u(\pi\pi)\ell^-\bar{\nu}_\ell$ predicted by MC is shown at the top of the stack. Relevant numbers extracted from the fit are shown in Table X. It can be seen that the numbers of $B^- \to \rho^0\ell^-\bar{\nu}_\ell$ and $\bar{B}^0 \to \rho^+\ell^-\bar{\nu}_\ell$ decays are in excellent agreement with those obtained from the M^2_{miss} distribution fit. The results show that for the $B^- \to \rho^0\ell^-\bar{\nu}_\ell$ decay, the inclusive component decaying into two pions is overestimated in the current MC scheme; at our present sensitivity, the yield is consistent with zero. The extracted number of $B^- \to f_2(1270)\ell^-\bar{\nu}_\ell$ decays is more than 5σ away from zero and almost 3 times larger than the ISGW2 model prediction, but we cannot claim that the peak in data around $1.3\ \mathrm{GeV}/c^2$ is completely saturated by $B^- \to f_2(1270)\ell^-\bar{\nu}_\ell$ decays, and to do this an additional

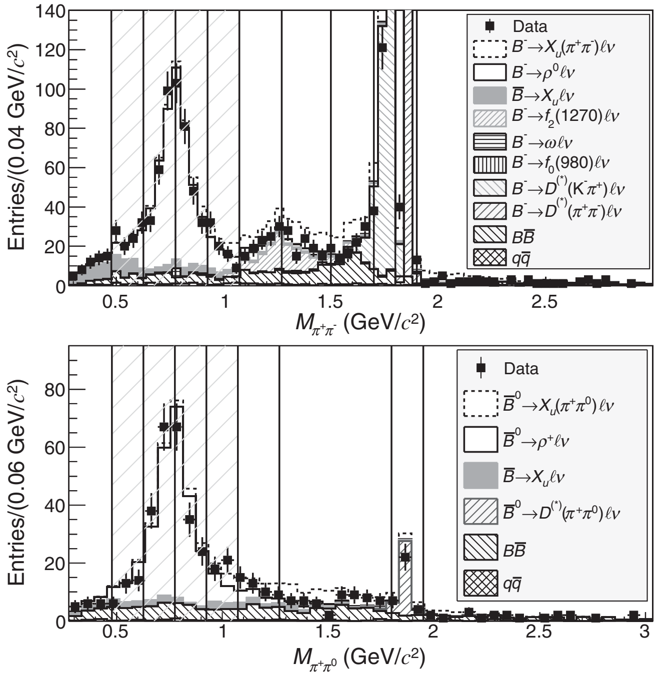

FIG. 11. Projection of the fitted distribution to data for the $\bar{B} \to \rho\ell^-\bar{\nu}_\ell$ decay onto the $M_{\pi\pi}$ axis. The top plot shows $B^- \to \rho^0\ell^-\bar{\nu}_\ell$; the bottom plot shows $\bar{B}^0 \to \rho^+\ell^-\bar{\nu}_\ell$. The inclusive component $\bar{B} \to X_u(\pi\pi)\ell^-\bar{\nu}_\ell$ predicted by MC is shown on the top of the stack. Vertical lines show the bins in invariant mass used during the fit procedure. The hatched region shows the actual selection criterion on the invariant mass.

dedicated study is needed. From the above, we estimate the uncertainty from the $\bar{B} \to X_u(\pi\pi)\ell^-\bar{\nu}_\ell$ nonresonant cross-feed to be 1%. For the $\bar{B}^0 \to \rho^+\ell^-\bar{\nu}_\ell$ decay, the fit cannot completely rule out a two-pion inclusive component, but it shows that it is overestimated in MC by at least a factor of 2. As a result of the fit, we estimate the uncertainty from the $\bar{B} \to X_u(\pi\pi)\ell^-\bar{\nu}_\ell$ cross-feed to be 5%. In light of the above, in this analysis we excluded the inclusive component that decays to two pions from the generated MC event samples.

The other backgrounds to the $B^- \to \rho^0\ell^-\bar{\nu}_\ell$ decay, $B^- \to \omega\ell^-\bar{\nu}_\ell$ where $\omega \to \pi^+\pi^-$ and $B^- \to f_0(980)\ell^-\bar{\nu}_\ell$ where $f_0 \to \pi^+\pi^-$, are expected to be small. Thus, we assign a conservative 100% uncertainty for the $B^- \to \omega\ell^-\bar{\nu}_\ell$ and $B^- \to f_0(980)\ell^-\bar{\nu}_\ell$ components, predicted by the MC simulation. We estimate the total uncertainty from X_u cross-feed to the $B^- \to \rho^0\ell^-\bar{\nu}_\ell$ decay branching fraction measurement to be 2.4%.

B. Cross-feed from $\bar{B}^0 \to \rho^+\ell^-\bar{\nu}_\ell$ to $\bar{B}^0 \to \pi^+\ell^-\bar{\nu}_\ell$ decays

There is a large cross-feed from $\bar{B}^0 \to \rho^+\ell^-\bar{\nu}_\ell$ to $\bar{B}^0 \to \pi^+\ell^-\bar{\nu}_\ell$ decays because those decays have an identical track topology, with one lepton and one charged pion on the signal side.

For the $\bar{B}^0 \to \pi^+\ell^-\bar{\nu}_\ell$ decay mode, the uncertainty in the $\bar{B}^0 \to \rho^+\ell^-\bar{\nu}_\ell$ cross-feed of 0.9% is estimated from the difference in the yields obtained from the $M^2_{\rm miss}$ fit where the $\bar{B}^0 \to \rho^+\ell^-\bar{\nu}_\ell$ component was first fixed using the PDG branching fraction value and then to the value obtained in this analysis.

In order to estimate how well the MC describes the shape of this background, we study the effect of vetoing events in the $\bar{B}^0 \to \pi^+\ell^-\bar{\nu}_\ell$ $M^2_{\rm miss}$ distribution that also pass the selection criteria for $\bar{B}^0 \to \rho^+\ell^-\bar{\nu}_\ell$ events. To suppress as many cross-feed events as possible, we use looser selection criteria to identify $\bar{B}^0 \to \rho^+\ell^-\bar{\nu}_\ell$ decays and compare this to the default selection. About 43% of MC generated $\bar{B}^0 \to \rho^+\ell^-\bar{\nu}_\ell$ decays are removed from the $\bar{B}^0 \to \pi^+\ell^-\bar{\nu}_\ell$ sample in this case. The ratio $N^{\rm DATA}/N^{\rm MC}$ changes by ~2% with an expected uncertainty of about 1.4% due to signal counting. We also observe that the veto changes the background shapes under the signal peak considerably, without introducing a significant effect on the data/MC ratio. We can therefore say that the MC reproduces the $\bar{B}^0 \to \rho^+\ell^-\bar{\nu}_\ell$ shapes sufficiently well to justify not assigning an additional systematic uncertainty due to this shape variation.

C. Continuum description

A check of the continuum description uncertainty is made using 79 fb^{-1} of off-peak data, collected at a collision energy 60 MeV below the $\Upsilon(4S)$ peak. It is difficult to

TABLE X. Results of the two-dimensional fit to the $M_{\pi\pi}$-$M^2_{\rm miss}$ distribution, for the scenarios where the $B \to X_u(\pi\pi)\ell\nu$ nonresonant component is either determined by the fit (top line for ρ^0 and ρ^+ fits) or set to zero in the fit (bottom line in each case). $N^{\rm fit}_{\pi\pi}$ and $N^{\rm MC}_{\pi\pi}$ are the numbers of $\bar{B} \to X_u(\pi\pi)\ell^-\bar{\nu}_\ell$ decays from the fit and MC prediction, respectively, N_{f_2} and $N^{\rm MC}_{f_2}$ are the numbers of $B^- \to f_2(1270)\ell^-\bar{\nu}_\ell$ decays from the fit and MC prediction, respectively, and $N^{\rm sel}_\rho$ is the number of $\bar{B} \to \rho\ell^-\bar{\nu}_\ell$ decays from the fit within the invariant mass selection criterion.

X_u	$N^{\rm fit}_{\pi\pi}$	$N^{\rm MC}_{\pi\pi}$	N_{f_2}	$N^{\rm MC}_{f_2}$	$N^{\rm sel}_\rho$
ρ^0	45.8 ± 45.4	334.9	128.0 ± 34.0	58.4	620.8 ± 34.4
	0		154.4 ± 22.2		627.0 ± 33.8
ρ^+	51.4 ± 23.0	125.6	N.A.		327.4 ± 27.8
	0				344.0 ± 27.8

TABLE XI. Comparison of the number of selected continuum events using loose criteria for the studied processes. $N_{q\bar{q}}^{\mathrm{MC}}$ is the MC prediction, and N^{data} is the number of off-peak data scaled according to the luminosity.

X_u	$N_{q\bar{q}}^{\mathrm{MC}}$	N^{DATA}	Ratio
π^0	1196 ± 15	1371 ± 110	0.87 ± 0.07
π^+	2982 ± 24	3045 ± 164	0.98 ± 0.05
ρ^0	3655 ± 27	3490 ± 176	1.05 ± 0.05
ρ^+	2999 ± 24	2561 ± 151	1.17 ± 0.07
$\omega(3\pi)$	401 ± 9	361 ± 57	1.11 ± 0.18
$\omega(\pi\gamma)$	234 ± 7	232 ± 45	1.01 ± 0.20

compare data and MC directly within the selection criteria used in the analysis because of the low off-peak sample size. We loosen the selection criteria on the $o_{\mathrm{tag}}^{\mathrm{cs}}$ and M_{bc} variables and compare yields and distributions between $q\bar{q}$ continuum MC and off-peak data. The total number of selected events for each studied decay mode is given in Table XI. A comparison of several distributions for the $B^- \to \rho^0 \ell^- \bar{\nu}_\ell$ decay is shown in Fig. 12. Decay distributions for other decay modes convey a similar picture. As can be seen, the data/MC agreement in most cases is at the level of 10%. Also, the M_{bc} and M_{miss}^2 distributions are found to be in good agreement.

It is difficult to claim that within the tighter, default selection criteria used in this analysis, the MC describes continuum events with the same level of agreement. Because of this, the uncertainty due to the continuum description is checked by scaling the continuum template histogram by a factor of 50% and examining the effect on the fits. Based on this, the systematic uncertainty due to the continuum description in MC is found to be less than 1% for all decay modes.

D. Model uncertainty

We estimate the uncertainty related to the form factor shape of $\bar{B} \to \pi \ell^- \bar{\nu}_\ell$ as the difference in efficiency when comparing the BCL [28] and KMOW [33] form factor parametrizations. For $\bar{B} \to \rho \ell^- \bar{\nu}_\ell$ and $B^- \to \omega \ell^- \bar{\nu}_\ell$ decays, we estimate the uncertainty as the difference in the total efficiencies obtained using the LCSR calculation [24] and the ISGW2 model result [25]. The $B^- \to \omega \ell^- \bar{\nu}_\ell$ decay has a slightly larger uncertainty than the other decays due to the steeper efficiency dependence on q^2.

E. Summary of systematic uncertainties

The summary of the systematic uncertainties is given in Table XII. The total uncertainty is obtained by summing the individual uncertainties in quadrature.

For branching fractions evaluated in bins of q^2, we assume for each source of systematic uncertainty (with model uncertainty excluded) that the size of the uncertainty is the same for all q^2 bins. As a consequence, the total systematic uncertainty is also assumed to be fully correlated between different q^2 bins; i.e., it does not affect the shape of the measured q^2 spectrum. As there is

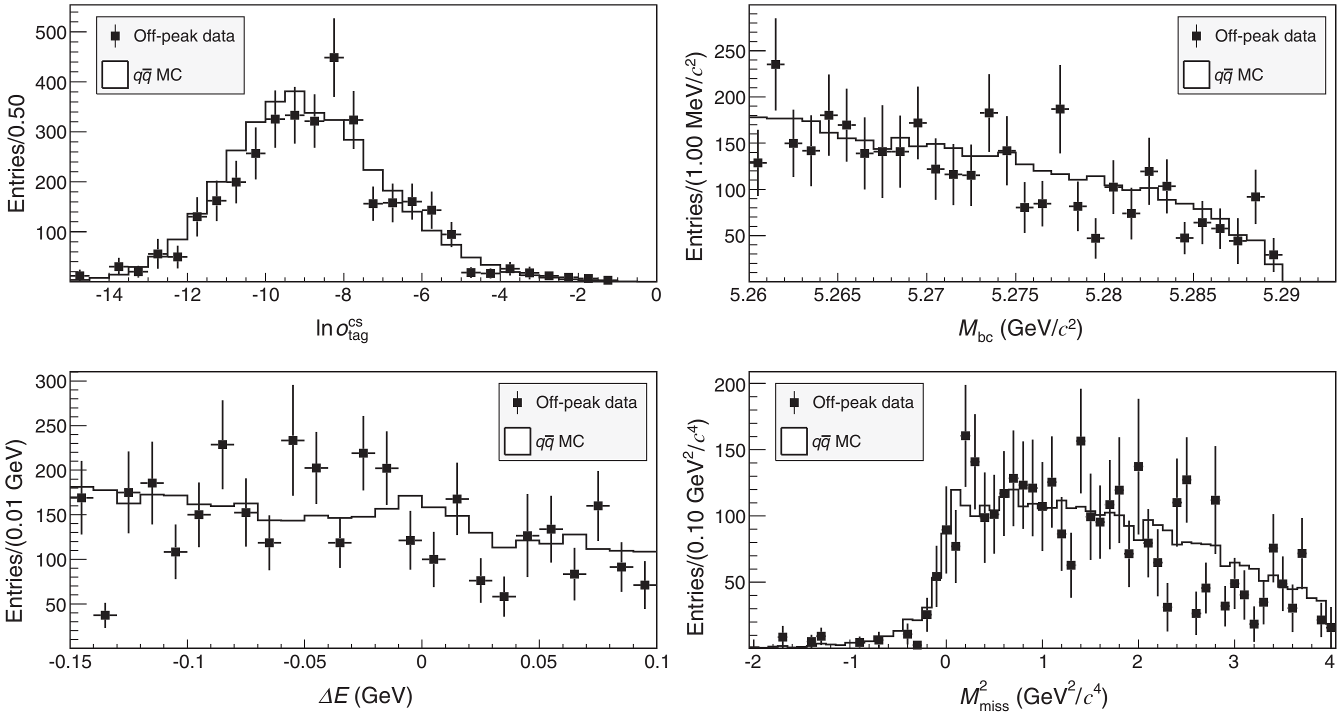

FIG. 12. Comparison of $q\bar{q}$ MC and off-peak data, using loose $B^- \to \rho^0 \ell^- \bar{\nu}_\ell$ decay selection criteria.

TABLE XII. Systematic uncertainties for the branching fraction results in percent.

Source of uncertainty	Assigned systematic uncertainty for $\bar{B} \to X_u \ell^- \bar{\nu}_\ell$ decays				
X_u	π^+	π^0	ρ^+	ρ^0	$\omega(3\pi)$
Detector simulation:					
Track reconstruction	0.35	-	0.35	0.7	0.7
π^0 reconstruction	-	2.0	2.0	-	2.0
Lepton identification	1.0	1.0	1.0	1.0	1.0
Kaon veto	0.9	-	1.0	2.0	2.0
Continuum description	1.0	0.5	0.5	0.7	0.0
X_u cross-feed	0.9	-	5.0	2.4	-
Tag calibration	4.5	4.2	4.5	4.2	4.2
Combined	4.9	4.8	7.2	5.4	5.2
Form factor shapes:	1.1	1.9	1.7	1.3	3.8
Total systematic error	5.0	5.1	7.4	5.6	6.4

one dominating source of systematic error—the tag calibration—this assumption should be valid to a good approximation.

To average between different isospin modes, we assume partial correlation in the tag efficiency calibration uncertainty (100% correlation in particle ID and 30% correlation in branching fraction uncertainties used for tag calibration), and 100% correlation in track reconstruction, lepton ID and kaon veto. The other components of the systematic uncertainty listed in Table XII are assumed to be uncorrelated. Under this assumption, the systematic correlation between the $\bar{B}^0 \to \pi^+ \ell^- \bar{\nu}_\ell$ and $B^- \to \pi^0 \ell^- \bar{\nu}_\ell$ modes is 49% and between the $\bar{B}^0 \to \rho^+ \ell^- \bar{\nu}_\ell$ and $B^- \to \rho^0 \ell^- \bar{\nu}_\ell$ modes 35%.

VIII. EXTRACTION OF $|V_{ub}|$

To extract a value for $|V_{ub}|$, we use the expression

$$|V_{ub}| = \sqrt{\frac{C_v \Delta \mathcal{B}}{\tau_B \Delta \zeta}}, \tag{30}$$

where $C_v = 2$ for B^+ decay modes and $C_v = 1$ for B^0 decay modes; τ_B is the lifetime of the corresponding B meson, $\Delta \mathcal{B}$ is the measured partial branching fraction within a given region of q^2 and $\Delta \zeta = \int d\Gamma / |V_{ub}|^2$ is the normalized partial decay width calculated within that q^2 region for each model. Values of $|V_{ub}|$ extracted from charmless semileptonic partial branching fractions within the q^2 region valid for each model are given in Table XIII. For low q^2, the form factor predictions are made using LCSR calculations while, for high q^2, the predictions are calculated using lattice QCD (LQCD). Some calculations give form factor predictions corresponding to the entire q^2 region. It is evident that the main contribution to the $|V_{ub}|$ uncertainty comes from theory. The experimental uncertainty is typically 2–3 times less than the corresponding theoretical one. The lifetime values $\tau_{B^0} = 1.519 \pm 0.007$ ps and $\tau_{B^+} = 1.641 \pm 0.008$ ps are taken from the PDG [5].

TABLE XIII. Values of the CKM matrix element $|V_{ub}|$ based on rates of exclusive $\bar{B} \to X_u \ell^- \bar{\nu}_\ell$ decays and theoretical predictions of form factors within various q^2 ranges. The first uncertainty is statistical, the second is experimental systematic and the third is theoretical. The theoretical uncertainty for the ISGW2 model is not available.

X_u	Theory	q^2, GeV/c^2	N^{fit}	N^{MC}	$\Delta\mathcal{B} \times 10^4$	$\Delta\zeta$, ps^{-1}	$\lvert V_{ub}\rvert \times 10^3$
π^0	LCSR [33]	<12	119.6 ± 16.2	116.5	0.423 ± 0.057	$4.59^{+1.00}_{-0.85}$	$3.35 \pm 0.23 \pm 0.09^{+0.36}_{-0.31}$
	LCSR [34]	<16	168.2 ± 18.9	153.5	0.588 ± 0.066	$5.44^{+1.43}_{-1.43}$	$3.63 \pm 0.20 \pm 0.10^{+0.60}_{-0.40}$
	HPQCD [35]	>16	58.6 ± 10.5	57.6	0.196 ± 0.035	$2.02^{+0.55}_{-0.55}$	$3.44 \pm 0.31 \pm 0.09^{+0.59}_{-0.39}$
	FNAL/MILC [36]					$2.21^{+0.47}_{-0.42}$	$3.29 \pm 0.30 \pm 0.09^{+0.37}_{-0.30}$
π^+	LCSR [33]	<12	247.2 ± 18.9	233.1	0.808 ± 0.062	$4.59^{+1.00}_{-0.85}$	$3.40 \pm 0.13 \pm 0.09^{+0.37}_{-0.32}$
	LCSR [34]	<16	324.2 ± 22.6	305.1	1.057 ± 0.074	$5.44^{+1.43}_{-1.43}$	$3.58 \pm 0.12 \pm 0.09^{+0.59}_{-0.39}$
	HPQCD [35]	>16	141.3 ± 16.0	116.1	0.445 ± 0.050	$2.02^{+0.55}_{-0.55}$	$3.81 \pm 0.22 \pm 0.10^{+0.66}_{-0.43}$
	FNAL/MILC [36]					$2.21^{+0.47}_{-0.42}$	$3.64 \pm 0.21 \pm 0.09^{+0.40}_{-0.33}$
ρ^0	LCSR [24]	<16	476.5 ± 30.5	420.0	1.431 ± 0.091	$13.7^{+3.4}_{-3.4}$	$3.56 \pm 0.11 \pm 0.09^{+0.54}_{-0.37}$
	Beyer/Melikhov [37]	full range	621.7 ± 35.0	505.1	1.834 ± 0.103	$15.8^{+2.3}_{-2.3}$	$3.76 \pm 0.11 \pm 0.10^{+0.31}_{-0.25}$
	UKQCD [38]					$16.5^{+3.5}_{-2.3}$	$3.68 \pm 0.10 \pm 0.10^{+0.29}_{-0.34}$
	ISGW2 [25]					14.1	$3.98 \pm 0.11 \pm 0.10$
ρ^+	LCSR [24]	<16	268.8 ± 25.0	245.7	2.574 ± 0.239	$13.7^{+3.4}_{-3.4}$	$3.51 \pm 0.16 \pm 0.13^{+0.53}_{-0.36}$
	Beyer/Melikhov [37]	full range	343.3 ± 28.3	295.1	3.222 ± 0.266	$15.8^{+2.3}_{-2.3}$	$3.66 \pm 0.15 \pm 0.14^{+0.30}_{-0.24}$
	UKQCD [38]					$16.5^{+3.5}_{-2.3}$	$3.59 \pm 0.15 \pm 0.13^{+0.28}_{-0.33}$
	ISGW2 [25]					14.1	$3.87 \pm 0.16 \pm 0.15$
$\omega(3\pi)$	LCSR [24]	<12	61.3 ± 11.4	71.6	0.611 ± 0.113	$7.88^{+1.86}_{-1.86}$	$3.08 \pm 0.29 \pm 0.11^{+0.44}_{-0.31}$
	ISGW2 [25]	full range	96.7 ± 14.5	104.1	1.069 ± 0.160	14.1	$3.03 \pm 0.23 \pm 0.11$

TABLE XIV. The elements B_{0k} calculated with $t_0 = t_{\rm opt}$ in units of 10^{-4}. The other elements can be obtained by the relation $B_{j(j+k)} = B_{0k}$ and the symmetry property $B_{jk} = B_{kj}$.

k	0	1	2	3	4	5	6	7	8	9	10	11	12	13	14
B_{0k}	197.08	41.93	−109.16	−58.89	−2.24	12.18	11.09	5.02	2.13	0.26	−0.07	−0.27	−0.16	−0.14	−0.07

We also perform a $|V_{ub}|$ determination with a model-independent description of $\bar B \to \pi\ell^-\bar\nu_\ell$ decays assuming isospin symmetry and the BCL form factor parametrization [28], the most recent LQCD calculation by the FNAL/MILC Collaboration [36], and the vector form factor value for $f_+(q^2)$ at $q^2 = 0$ calculated in the LCSR framework from [39]. We define a goodness of fit as follows:

$$\chi^2 = \chi^2_{\bar B\to\pi\ell^-\bar\nu_\ell} + \chi^2_{\rm LCSR} + \chi^2_{\rm LQCD}. \tag{31}$$

Here, χ^2 for the $\bar B^0 \to \pi^+\ell^-\bar\nu_\ell$ and $B^- \to \pi^0\ell^-\bar\nu_\ell$ decay modes is given by

$$\chi^2_{\bar B\to\pi\ell^-\bar\nu_\ell} = \sum_{i,j}\delta\mathcal{B}_i (C^{\rm EXP})^{-1}_{ij}\delta\mathcal{B}_j, \tag{32}$$

where $C^{\rm EXP} = C^{\rm EXP}_{\rm stat} + C^{\rm EXP}_{\rm syst}$ is the full experimental variance matrix. The statistical variance matrix $C^{\rm EXP}_{\rm stat}$ is presented in the Appendix. The systematic variance matrix $C^{\rm EXP}_{\rm syst}$ is obtained from the uncertainties given in Table XII, excluding the form factor shape uncertainty.

The difference between the measured and predicted partial branching fractions $\delta\mathcal{B}_i$ in the q^2 range Δq_i^2 is given by

$$\delta\mathcal{B}_i = \mathcal{B}_i^{\rm exp} - \frac{\tau_B}{C_v}\int_{\Delta q_i^2}\frac{G_F^2}{24\pi^3}|V_{ub}|^2|f_+(q^2,\vec b)|^2|\vec p_\pi|^3{\rm d}q^2, \tag{33}$$

where $C_v = 2$ for $B^- \to \pi^0\ell^-\bar\nu_\ell$ and $C_v = 1$ for $\bar B^0 \to \pi^+\ell^-\bar\nu_\ell$, and $f_+(q^2,\vec b)$ is expressed using the BCL form factor parametrization [28]:

$$f_+(q^2,\vec b) = \frac{1}{1 - q^2/m^2_{B^*}}\sum_{k=0}^{K} b_k(t_0)z(q^2)^k. \tag{34}$$

The factor in front of the sum describes the pole due to the presence of the B^* vector resonance with mass $m_{B^*} = 5.325\ {\rm GeV}/c^2$; the vector $\vec b = (b_0, b_1, b_2, \ldots, b_K)$ for a chosen value of K represents the set of parameters to be determined by the fit. The function $z(q^2) \equiv z(q^2, t_0)$ is given by

$$z(q^2,t_0) = \frac{\sqrt{t_+ - q^2} - \sqrt{t_+ - t_0}}{\sqrt{t_+ - q^2} + \sqrt{t_+ - t_0}}, \tag{35}$$

where $t_+ = (m_B + m_\pi)^2$ and the optimal choice for t_0 is $t_0 = t_{\rm opt} \equiv (m_B + m_\pi)(\sqrt{m_B} - \sqrt{m_\pi})^2$, which provides a mapping of the physical region $0 < q^2 < (m_B - m_\pi)^2$ onto the symmetric interval $|z| < 0.279$ in the complex z plane. The last parameter b_K in the vector $\vec b$ is constrained by angular momentum conservation at the $B\pi$ threshold:

$$b_K = -\frac{(-1)^K}{K}\sum_{k=0}^{K-1}(-1)^k k b_k, \tag{36}$$

leaving only $(b_0, b_1, b_2, \ldots, b_{K-1})$ free. Unitarity and crossing symmetry properties of the form factor constrain the $\vec b$ parameters:

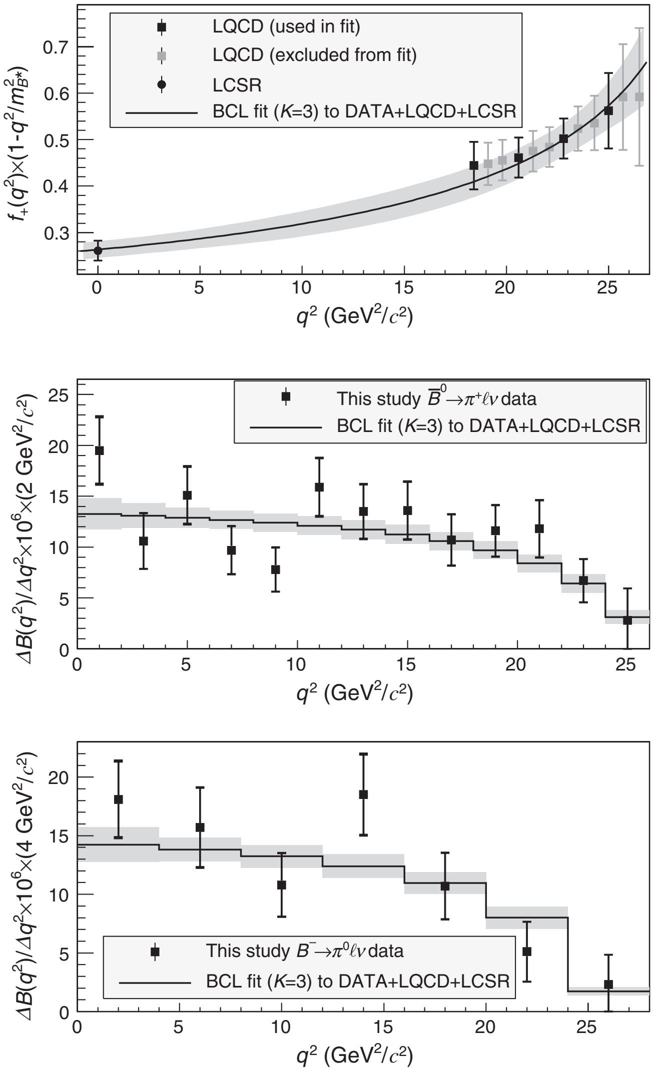

FIG. 13. Fit to data obtained in this analysis, LQCD points and the LCSR prediction at $q^2 = 0$ using the BCL parametrization, with the number of free parameters $N = 4$. The shaded regions represent the uncertainties of the fit.

TABLE XV. The fit results for different numbers of parameters N and various sets of data with full reconstruction tagging and theoretical predictions. The "+" sign indicates that the corresponding data set was included in the fit and the "−" sign otherwise.

N	LCSR	LQCD	$\pi^+\ell^-\bar{\nu}_\ell$	$\pi^0\ell^-\bar{\nu}_\ell$	b_0	b_1	b_2	$\lvert V_{ub}\rvert \times 10^3$	$\sum B_{jk}b_jb_k$	χ^2/ndf
3	+	+	+	+	0.450 ± 0.030	-0.588 ± 0.081		3.40 ± 0.23	0.0146	22.82/22
3	−	+	+	+	0.455 ± 0.039	-0.586 ± 0.083		3.35 ± 0.35	0.0146	22.79/21
3	+	−	+	+	0.444 ± 0.054	-0.575 ± 0.131		3.44 ± 0.35	0.0141	22.53/18
3	+	+	−	+	0.439 ± 0.032	-0.530 ± 0.098		3.50 ± 0.27	0.0125	6.36/9
3	+	+	+	−	0.459 ± 0.031	-0.635 ± 0.090		3.39 ± 0.24	0.0165	16.11/15
3	−	+	−	+	0.462 ± 0.040	-0.467 ± 0.126		3.17 ± 0.41	0.0110	5.40/8
3	−	+	+	−	0.451 ± 0.039	-0.645 ± 0.092		3.50 ± 0.39	0.0167	15.97/14
3	+	−	−	+	0.379 ± 0.063	-0.369 ± 0.173		3.83 ± 0.45	0.0071	5.07/5
3	+	−	+	−	0.485 ± 0.067	-0.702 ± 0.176		3.27 ± 0.36	0.0197	15.60/11
4	+	+	+	+	0.438 ± 0.033	-0.701 ± 0.162	0.171 ± 0.577	3.52 ± 0.29	0.0152	22.20/21
4	−	+	+	+	0.443 ± 0.041	-0.700 ± 0.164	0.177 ± 0.583	3.47 ± 0.40	0.0153	22.16/20
4	+	−	+	+	0.427 ± 0.051	-0.802 ± 0.225	0.566 ± 0.685	3.65 ± 0.40	0.0299	21.18/17
4	+	+	−	+	0.437 ± 0.038	-0.545 ± 0.197	-0.198 ± 0.745	3.52 ± 0.33	0.0115	6.35/8
4	+	+	+	−	0.446 ± 0.035	-0.756 ± 0.177	0.190 ± 0.643	3.53 ± 0.31	0.0177	15.51/14
4	−	+	−	+	0.457 ± 0.042	-0.517 ± 0.207	0.005 ± 0.777	3.19 ± 0.43	0.0090	5.31/7
4	−	+	+	−	0.438 ± 0.042	-0.760 ± 0.174	0.171 ± 0.640	3.63 ± 0.45	0.0176	15.40/13
4	+	−	−	+	0.378 ± 0.064	-0.380 ± 0.414	-0.145 ± 1.286	3.84 ± 0.55	0.0066	5.07/4
4	+	−	+	−	0.454 ± 0.061	-1.008 ± 0.263	0.875 ± 0.798	3.58 ± 0.43	0.0580	13.69/10

$$\sum_{j,k=0}^{K} B_{jk} b_j b_k \leq 1, \tag{37}$$

where the coefficients B_{0k}, $0 \leq k \leq 14$ are given in Table XIV.

The contribution to the χ^2 function from the LQCD points is

$$\chi^2_{\mathrm{LQCD}} = \sum_{i,j} \delta f_+^{\mathrm{LQCD}}(q_i^2)(C^{\mathrm{LQCD}})^{-1}_{ij} \delta f_+^{\mathrm{LQCD}}(q_j^2), \tag{38}$$

where C^{LQCD} is the full variance matrix provided with the LQCD points $f_+^{\mathrm{LQCD}}(q_i^2)$, and

$$\delta f_+^{\mathrm{LQCD}}(q_i^2) = f_+^{\mathrm{LQCD}}(q_i^2) - f_+(q_i^2, \vec{b}). \tag{39}$$

The LQCD points are highly correlated, and more than half of the eigenvalues of the LQCD covariance matrix are extremely small (of the order of 10^{-6} of the largest eigenvalue) or even negative. To treat this situation, we omit some of the LQCD points as suggested in Ref. [8], leaving only 4 points out of 12. This allows us to build the contribution to the χ^2 from LQCD data.

The LCSR contribution to the total χ^2 is

$$\chi^2_{\mathrm{LCSR}} = \left(\frac{f_+^{\mathrm{LCSR}}(0) - f_+(0, \vec{b})}{\delta f_+^{\mathrm{LCSR}}(0)}\right)^2, \tag{40}$$

where $f_+^{\mathrm{LCSR}}(0) = 0.261^{+0.020}_{-0.023}$ from [39]. In this formalism, the free parameters are $|V_{ub}|$ and the real coefficients b_k, $0 \leq k < K$; thus, the total number of free parameters is $N = K + 1$.

A typical fit is shown in Fig. 13, using $\bar{B}^0 \to \pi^+\ell^-\bar{\nu}_\ell$ and $B^- \to \pi^0\ell^-\bar{\nu}_\ell$ data, LQCD points and the LCSR form factor prediction at $q^2 = 0$ with $N = 4$.

The fit results obtained using different numbers of parameters in the BCL parametrization, along with all possible combinations of $\bar{B}^0 \to \pi^+\ell^-\bar{\nu}_\ell$ and $B^- \to \pi^0\ell^-\bar{\nu}_\ell$ differential branching fractions obtained in this analysis, as well as the theoretical predictions, are shown in Table XV. It can be seen that the values of $|V_{ub}|$ are in agreement for the different data sets, indicating that the input data are self-consistent at the current level of precision. For $N > 4$, the form factor parametrization starts to oscillate, reflecting the statistical fluctuations in the data, and does not satisfy the unitarity condition on the parameters $\sum B_{jk}b_jb_k \leq 1$.

To estimate the effect of truncating the series in z, we use the most recent untagged Belle [13] and *BABAR* [12] data, which have better statistical and completely different systematic uncertainties. An example of the combined fit is shown in Fig. 14, with $N = 6$, the largest number of parameters where the unitarity condition is not saturated. For larger numbers of parameters, we artificially force the unitarity condition by adding a component to the χ^2 function that is zero if the unitarity condition is not saturated and steeply rising to infinity when approaching the unitarity bound:

$$\chi^2_{\mathrm{unitarity}} = \frac{1}{1 - u^{150}} - 1, \qquad u = \sum_{j,k=0}^{K} B_{jk} b_j b_k. \tag{41}$$

The values of $|V_{ub}|$ extracted using different numbers of terms in the form factor expansion are shown in Table XVI. To be sure that the χ^2 minimum is a true minimum, we

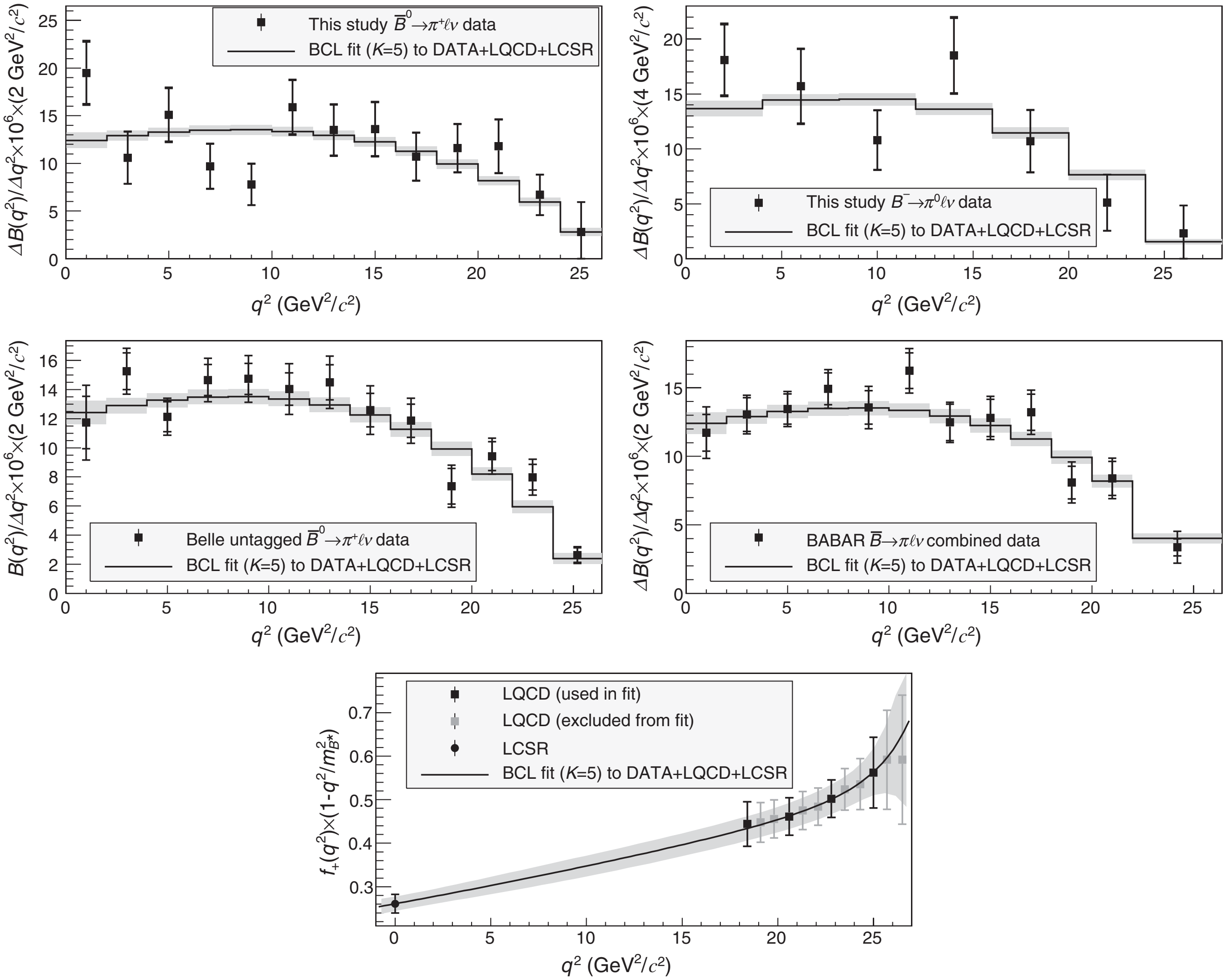

FIG. 14. The combined fit to the most recent data and theory inputs using the BCL parametrization with the number of free parameters $N = 6$ using untagged Belle [13] and *BABAR* [12] and tagged (this study) data. Shaded regions represent the uncertainties of the fit.

TABLE XVI. Fit results with different numbers of free parameters N and forced unitarity bound on the coefficients of the expansion using untagged Belle [13], *BABAR* [12] and tagged (this study) data and the LCSR and LQCD calculations. Note that in this approach the $|V_{ub}|$ error cannot be reliably estimated for $N > 6$ near the unitarity bound.

N	$\lvert V_{ub}\rvert\times10^3$	$\sum B_{jk}b_jb_k$	χ^2/ndf
3	3.47 ± 0.21	0.0148	46.39/47
4	3.41 ± 0.22	0.0232	45.37/46
5	3.39 ± 0.22	0.1073	44.76/45
6	3.39 ± 0.22	0.2289	44.74/44
7	3.39 ± 0.20	0.9501	44.65/43
8	3.39 ± 0.08	0.9503	44.65/42
9	3.39 ± 0.09	0.9525	44.62/41
10	3.39 ± 0.09	0.9525	44.62/40
11	3.39 ± 0.09	0.9527	44.59/39
12	3.39 ± 0.11	0.9531	44.59/38
13	3.39 ± 0.09	0.9538	44.58/37
14	3.39 ± 0.10	0.9539	44.58/36
15	3.39 ± 0.09	0.9545	44.56/35

repeated the fit many times, starting with a random initial vector of parameters $\vec{b}$ that satisfies the unitarity condition. It can be seen from Table XVI that the value of $|V_{ub}|$ is stable starting from $N = 4$; additional parameters only slightly improve the overall χ^2. From this, we can conclude that the number of terms in the expansion, $K = N - 1 = 3$, is enough to describe the current data with a negligibly small, ~0.5%, systematic uncertainty due to unaccounted terms in the expansion.

As a result of the model-independent fit of both the $\bar{B}^0\to\pi^+\ell^-\bar{\nu}_\ell$ and $B^-\to\pi^0\ell^-\bar{\nu}_\ell$ differential branching fractions measured in this analysis, the LQCD form factor points and LCSR prediction with $N = 4$, we quote $|V_{ub}| = (3.52\pm0.29)\times10^{-3}$. It is difficult to unequivocally separate the experimental and theoretical uncertainties so we quote only a total error. Using only the LCSR prediction or LQCD points in the fit as shown in Table XV, we can conclude that the LCSR prediction and LQCD points have almost equal contributions to the total uncertainty.

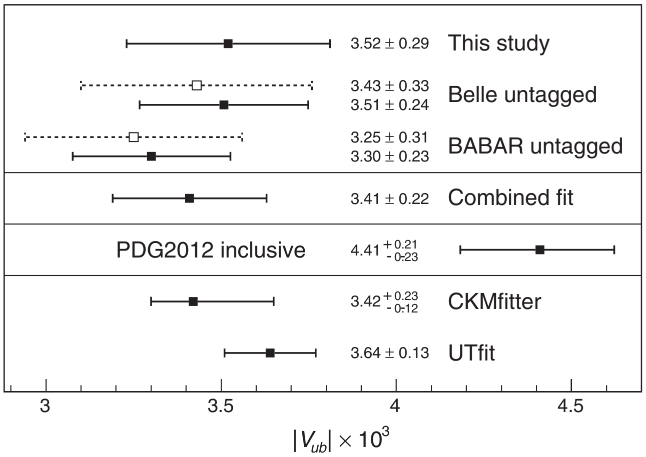

FIG. 15. The comparison of $|V_{ub}|$ values obtained with the BCL form factor parametrization with the number of terms in expansion $K = 3$, using LCSR and LQCD inputs for tagged (this analysis), untagged Belle [13] and *BABAR* [12] data as well as a combined fit with those three data sets. The value of $|V_{ub}|$ based on inclusive semileptonic decays of B mesons is taken from the recent PDG [5] review. The CKMfitter [40] and UTfit [41] estimates of $|V_{ub}|$ are from global fits where $|V_{ub}|$ related inputs are excluded. The dashed lines represent $|V_{ub}|$ values quoted in the original papers.

In Fig. 15, we show the value of $|V_{ub}|$ obtained in this analysis, compared to values obtained from other recent measurements and global determinations. The extracted value of $|V_{ub}|$ has comparable precision to, and agrees with, the values obtained from untagged Belle [13] and *BABAR* [12] data using the same method of determination as in this analysis. The figure shows both the values quoted in the Belle and *BABAR* papers and the values obtained by refitting using the original data and the method used in the present analysis. The combined fit shown uses data from all three analyses. Our value is also in agreement with the results of global fits performed by the CKMfitter [40] and UTfit [41] groups, where they excluded $|V_{ub}|$ related inputs from the fits. The tension between the value of $|V_{ub}|$ extracted from $\bar{B} \to \pi \ell^- \bar{\nu}_\ell$ decays and that measured in inclusive semileptonic decays of B mesons, represented in the figure by the latest PDG [5] value, remains significant ($\sim 3\sigma$).

We note that all theoretical predictions used in $|V_{ub}|$ extraction procedures described above assume no photon emission in the final state. For future experiments with much larger data samples, it will become crucial for theory to take into account radiative effects to describe high precision experimental data.

IX. CONCLUSION

We measure the total branching fractions for $B^- \to \pi^0 \ell^- \bar{\nu}_\ell$, $\bar{B}^0 \to \pi^+ \ell^- \bar{\nu}_\ell$, $B^- \to \rho^0 \ell^- \bar{\nu}_\ell$, $\bar{B}^0 \to \rho^+ \ell^- \bar{\nu}_\ell$ and $B^- \to \omega \ell^- \bar{\nu}_\ell$ decays using fully reconstructed hadronic B decays as a tag. This technique provides exceptionally clean signal samples and thus low systematic uncertainty in the final results. The $B^- \to \pi^0 \ell^- \bar{\nu}_\ell$ and $\bar{B}^0 \to \pi^+ \ell^- \bar{\nu}_\ell$ branching fractions are in good agreement with the previous Belle result [13] using an untagged reconstruction technique and with the recent *BABAR* measurement [12], and also with the isospin symmetry relation. The $B^- \to \rho^0 \ell^- \bar{\nu}_\ell$ and $\bar{B}^0 \to \rho^+ \ell^- \bar{\nu}_\ell$ branching fractions are also in good agreement with the isospin symmetry relation. The $\bar{B} \to \rho \ell^- \bar{\nu}_\ell$ branching fraction is 43% (2.7σ) higher than the PDG value and its precision is almost a factor of 2 better. This raises the probability that, in the previous analyses, backgrounds to $\bar{B} \to \rho \ell^- \bar{\nu}_\ell$ decays may have been considerably overestimated.

For the first time, we have an indication of neutral charmless hadronic states above 1 GeV$/c^2$ in invariant mass in semileptonic decays of B mesons. The broad peak observed in the $\pi^+\pi^-$ invariant mass distribution around 1.3 GeV$/c^2$ is dominated in our fit by the $B^- \to f_2(1270) \ell^- \bar{\nu}_\ell$ decay where $f_2 \to \pi^+\pi^-$. The fitted yield is 2–3 times higher than expected from the ISGW2 model and, assuming the absence of the nonresonant $\bar{B} \to X_u(\pi\pi) \ell^- \bar{\nu}_\ell$ decay, it has high statistical significance. A dedicated study is needed to fully explore the region above 1 GeV$/c^2$.

From the studied decays, we extract values of $|V_{ub}|$ in various q^2 regions where the theoretical predictions of the hadronic form factors are valid. The resulting values of $|V_{ub}|$ are in good agreement with each other. We also measure the q^2 dependence of the partial branching fractions, which can be used to test the theoretical predictions for the hadronic form factors.

For the $\bar{B} \to \pi \ell^- \bar{\nu}_\ell$ decay, we extract a value of $|V_{ub}| = (3.52 \pm 0.29) \times 10^{-3}$ using our measured partial branching fractions, a recent LCSR calculation, LQCD points and a model-independent description of the $f_+(q^2)$ hadronic form factor. We also present values of $|V_{ub}|$ obtained from fits where we do not assume that the theoretical inputs from LCSR and LQCD can be included in the same fit. Within the BCL parametrization, we have shown that three terms in the z expansion are enough to extract a value of $|V_{ub}|$ with negligibly small systematic uncertainty due to truncating the expansion.

ACKNOWLEDGMENTS

We thank the KEKB group for the excellent operation of the accelerator; the KEK cryogenics group for the efficient operation of the solenoid; and the KEK computer group, the National Institute of Informatics, and the PNNL/EMSL computing group for valuable computing and SINET4 network support. We acknowledge support from the Ministry of Education, Culture, Sports, Science, and Technology (MEXT) of Japan, the Japan Society for the Promotion of Science (JSPS), and the Tau-Lepton Physics Research Center of Nagoya University; the Australian Research Council and the Australian Department of

Industry, Innovation, Science and Research; Austrian Science Fund under Grant No. P 22742-N16; the National Natural Science Foundation of China under Contracts No. 10575109, No. 10775142, No. 10875115 and No. 10825524; the Ministry of Education, Youth and Sports of the Czech Republic under Contract No. MSM0021620859; the Carl Zeiss Foundation, the Deutsche Forschungsgemeinschaft and the VolkswagenStiftung; the Department of Science and Technology of India; the Istituto Nazionale di Fisica Nucleare of Italy; The BK21 and WCU program of the Ministry of Education, Science and Technology, National Research Foundation of Korea Grants No. 2010-0021174, No. 2011-0029457, No. 2012-0008143, and No. 2012R1A1A2008330, the BRL program under NRF Grant No. KRF-2011-0020333, and GSDC of the Korea Institute of Science and Technology Information; the Polish Ministry of Science and Higher Education and the National Science Center; the Ministry of Education and Science of the Russian Federation and the Russian Federal Agency for Atomic Energy; the Slovenian Research Agency; the Basque Foundation for Science (IKERBASQUE) and the UPV/EHU under program UFI 11/55; the Swiss National Science Foundation; the National Science Council and the Ministry of Education of Taiwan; and the U.S. Department of Energy and the National Science Foundation. This work is supported by a Grant-in-Aid from MEXT for Science Research in a Priority Area (“New Development of Flavor Physics”), and from JSPS for Creative Scientific Research (“Evolution of Tau-lepton Physics”).

APPENDIX

In this appendix, we present the fitted event yields, unfolded yields, efficiencies and corresponding partial branching fractions for the decays investigated in this study, in bins of q^2, in Tables XVII, XIX, XXI, XXIII, and XXV. We also give the statistical correlations between q^2 bins in Tables XVIII, XX, XXII, XXIV, and XXVI.

TABLE XVII. Raw $\bar{B}^0 \to \pi^+ \ell^- \bar{\nu}_\ell$ yields obtained from the two-dimensional fit, unfolded yields, efficiencies and partial branching fractions in bins of q^2.

Δq^2, GeV$^2/c^2$	$N_{\rm fit}$	$N_{\rm fit}^{\rm unfolded}$	ε, 10^{-3}	$\Delta\mathcal{B}$, 10^{-6}
0–2	53.9 ± 8.6	55.5 ± 9.2	1.90 ± 0.07	19.5 ± 3.2
2–4	35.4 ± 7.5	33.0 ± 8.4	2.07 ± 0.07	10.6 ± 2.7
4–6	42.5 ± 7.3	44.5 ± 8.2	1.96 ± 0.06	15.1 ± 2.8
6–8	30.5 ± 6.6	29.8 ± 7.2	2.05 ± 0.06	9.7 ± 2.3
8–10	27.2 ± 6.4	25.1 ± 6.9	2.14 ± 0.06	7.8 ± 2.2
10–12	48.9 ± 8.2	50.7 ± 9.0	2.13 ± 0.06	15.9 ± 2.8
12–14	43.0 ± 7.8	43.0 ± 8.5	2.13 ± 0.06	13.5 ± 2.7
14–16	40.7 ± 7.9	41.2 ± 8.5	2.02 ± 0.06	13.6 ± 2.8
16–18	34.0 ± 7.5	34.6 ± 8.0	2.16 ± 0.07	10.7 ± 2.5
18–20	39.7 ± 8.2	40.1 ± 8.7	2.31 ± 0.09	11.6 ± 2.5
20–22	35.6 ± 8.0	36.4 ± 8.6	2.06 ± 0.12	11.8 ± 2.8
22–24	21.6 ± 6.3	21.5 ± 6.8	2.14 ± 0.21	6.7 ± 2.1
24–26	8.0 ± 6.3	5.6 ± 6.3	1.35 ± 0.39	2.8 ± 3.1
Full range	461.1 ± 27.4	461.1 ± 27.4	2.07 ± 0.02	149.4 ± 9.1

TABLE XVIII. Normalized statistical correlation matrix in percent for the $\bar{B}^0 \to \pi^+ \ell^- \bar{\nu}_\ell$ partial branching fractions.

Δq^2, GeV$^2/c^2$	0–2	2–4	4–6	6–8	8–10	10–12	12–14	14–16	16–18	18–20	20–22	22–24	24–26
0–2	100.0	−14.5	1.0	−0.1	0.0	0.0	0.0	0.0	0.0	−0.0	−0.0	0.1	0.1
2–4	−14.5	100.0	−10.0	0.8	−0.0	0.1	−0.2	−0.1	−0.1	0.1	−0.1	−0.0	0.0
4–6	1.0	−10.0	100.0	−9.4	0.3	−0.1	0.0	0.1	0.1	−0.2	−0.2	0.0	0.4
6–8	−0.1	0.8	−9.4	100.0	−7.8	0.5	0.0	0.0	0.1	−0.1	0.2	0.2	0.5
8-10	0.0	−0.0	0.3	−7.8	100.0	−9.7	0.3	0.1	0.1	0.0	0.4	0.3	0.9
10–12	0.0	0.1	−0.1	0.5	−9.7	100.0	−7.2	0.5	0.1	0.3	0.5	0.4	1.3
12–14	0.0	−0.2	0.0	0.0	0.3	−7.2	100.0	−6.2	0.4	0.2	0.1	0.2	1.0
14–16	0.0	−0.1	0.1	0.0	0.1	0.5	−6.2	100.0	−5.9	0.2	0.3	0.2	1.1
16–18	0.0	−0.1	0.1	0.1	0.1	0.1	0.4	−5.9	100.0	−4.7	0.1	−0.0	0.9
18–20	−0.0	0.1	−0.2	−0.1	0.0	0.3	0.2	0.2	−4.7	100.0	−1.8	0.2	0.5
20–22	−0.0	−0.1	−0.2	0.2	0.4	0.5	0.1	0.3	0.1	−1.8	100.0	−5.5	−2.0
22–24	0.1	−0.0	0.0	0.2	0.3	0.4	0.2	0.2	−0.0	0.2	−5.5	100.0	−1.2
24–26	0.1	0.0	0.4	0.5	0.9	1.3	1.0	1.1	0.9	0.5	−2.0	−1.2	100.0

TABLE XIX. Raw $B^- \to \pi^0 \ell^- \bar{\nu}_\ell$ yields obtained from the two-dimensional fit, unfolded yields, efficiencies and partial branching fractions in bins of q^2.

Δq^2, GeV^2/c^2	N_{fit}	$N_{\mathrm{fit}}^{\mathrm{unfolded}}$	ε, 10^{-3}	$\Delta\mathcal{B}$, 10^{-6}
0–4	45.2 ± 7.8	50.2 ± 8.9	1.76 ± 0.06	18.1 ± 3.2
4–8	45.9 ± 8.2	44.7 ± 9.6	1.80 ± 0.06	15.7 ± 3.4
8–12	35.1 ± 7.2	33.8 ± 8.4	1.99 ± 0.06	10.8 ± 2.7
12–16	51.7 ± 8.7	54.2 ± 10.0	1.86 ± 0.06	18.5 ± 3.4
16–20	33.1 ± 7.3	32.3 ± 8.5	1.93 ± 0.07	10.7 ± 2.8
20–24	16.3 ± 6.0	13.5 ± 6.8	1.69 ± 0.14	5.1 ± 2.6
24–28	6.1 ± 4.4	4.5 ± 5.0	1.24 ± 0.51	2.3 ± 2.5
Full range	233.3 ± 20.6	233.3 ± 20.6	1.83 ± 0.03	81.2 ± 7.4

TABLE XX. Normalized statistical correlation matrix in percent for the $B^- \to \pi^0 \ell^- \bar{\nu}_\ell$ partial branching fractions.

Δq^2, GeV^2/c^2	0–4	4–8	8–12	12–16	16–20	20–24	24–28
0–4	100.0	−15.9	3.5	1.2	1.3	1.6	2.1
4–8	−15.9	100.0	−14.9	3.0	1.3	1.5	2.5
8–12	3.5	−14.9	100.0	−9.8	3.4	2.8	4.2
12–16	1.2	3.0	−9.8	100.0	−11.2	2.8	3.5
16–20	1.3	1.3	3.4	−11.2	100.0	−11.5	2.6
20–24	1.6	1.5	2.8	2.8	−11.5	100.0	−13.1
24–28	2.1	2.5	4.2	3.5	2.6	−13.1	100.0

TABLE XXI. Raw $\bar{B}^0 \to \rho^+ \ell^- \bar{\nu}_\ell$ yields obtained from the two-dimensional fit, unfolded yields, efficiencies and partial branching fractions in bins of q^2.

Δq^2, GeV^2/c^2	N_{fit}	$N_{\mathrm{fit}}^{\mathrm{unfolded}}$	ε, 10^{-4}	$\Delta\mathcal{B}$, 10^{-6}
0–4	35.5 ± 9.3	37.2 ± 10.6	6.76 ± 0.19	37.3 ± 10.6
4–8	72.1 ± 10.5	76.2 ± 12.3	7.20 ± 0.18	71.8 ± 11.6
8–12	88.1 ± 11.9	90.0 ± 13.7	7.58 ± 0.17	80.6 ± 12.3
12–16	80.2 ± 11.9	78.0 ± 13.5	7.32 ± 0.18	72.3 ± 12.5
16–20	69.4 ± 11.2	67.6 ± 12.4	7.33 ± 0.22	62.6 ± 11.5
20–24	4.9 ± 4.7	1.1 ± 5.2	4.43 ± 0.62	1.7 ± 7.9
Full range	350.2 ± 27.3	350.2 ± 27.3	7.22 ± 0.09	326.2 ± 26.3

TABLE XXII. Normalized statistical correlation matrix in percent for the $\bar{B}^0 \to \rho^+ \ell^- \bar{\nu}_\ell$ partial branching fractions.

Δq^2, GeV^2/c^2	0–4	4–8	8–12	12–16	16–20	20–24
0–4	100.0	−14.1	2.4	0.9	1.1	1.6
4–8	−14.1	100.0	−11.2	3.0	2.4	2.5
8–12	2.4	−11.2	100.0	−7.5	5.0	5.8
12–16	0.9	3.0	−7.5	100.0	−8.8	6.1
16–20	1.1	2.4	5.0	−8.8	100.0	−10.2
20–24	1.6	2.5	5.8	6.1	−10.2	100.0

TABLE XXIII. Raw $B^- \to \rho^0 \ell^- \bar{\nu}_\ell$ yields obtained from the two-dimensional fit, unfolded yields, efficiencies and partial branching fractions in bins of q^2.

Δq^2, GeV^2/c^2	N_{fit}	$N_{\mathrm{fit}}^{\mathrm{unfolded}}$	ε, 10^{-3}	$\Delta\mathcal{B}$, 10^{-6}
0–2	35.7 ± 9.2	36.6 ± 10.0	1.85 ± 0.06	12.4 ± 3.4
2–4	52.6 ± 9.4	52.1 ± 10.4	2.14 ± 0.06	15.3 ± 3.1
4–6	55.5 ± 9.3	55.4 ± 10.5	1.95 ± 0.06	17.9 ± 3.4
6–8	70.2 ± 10.2	72.4 ± 11.3	2.10 ± 0.06	21.7 ± 3.4
8–10	52.6 ± 9.2	50.7 ± 10.3	2.23 ± 0.06	14.3 ± 2.9
10–12	66.7 ± 10.4	67.0 ± 11.6	2.12 ± 0.06	19.9 ± 3.4
12–14	75.3 ± 10.6	77.9 ± 11.8	2.18 ± 0.06	22.4 ± 3.4
14–16	77.4 ± 11.1	78.7 ± 12.1	2.28 ± 0.06	21.7 ± 3.3
16–18	64.8 ± 10.7	63.1 ± 11.4	2.27 ± 0.07	17.5 ± 3.2
18–20	52.3 ± 9.5	51.7 ± 10.2	2.27 ± 0.09	14.3 ± 2.8
20–22	18.9 ± 6.9	16.3 ± 7.1	1.74 ± 0.17	5.9 ± 2.6
Full range	621.9 ± 34.8	621.9 ± 34.8	2.13 ± 0.02	183.5 ± 10.4

TABLE XXIV. Normalized statistical correlation matrix in percent for the $B^- \to \rho^0 \ell^- \bar{\nu}_\ell$ partial branching fractions.

Δq^2, GeV^2/c^2	0–2	2–4	4–6	6–8	8–10	10–12	12–14	14–16	16–18	18–20	20–22
0–2	100.0	−12.3	0.8	0.0	0.2	0.2	0.2	0.3	0.3	0.3	0.3
2–4	−12.3	100.0	−10.9	0.8	0.5	0.5	0.6	0.7	0.9	0.8	0.8
4–6	0.8	−10.9	100.0	−9.7	0.9	0.9	0.8	0.9	1.3	1.1	1.1
6–8	0.0	0.8	−9.7	100.0	−8.8	1.4	1.2	1.5	1.8	1.4	1.6
8–10	0.2	0.5	0.9	−8.8	100.0	−9.3	1.5	1.6	2.1	1.7	1.8
10–12	0.2	0.5	0.9	1.4	−9.3	100.0	−6.6	1.9	2.7	2.3	2.4
12–14	0.2	0.6	0.8	1.2	1.5	−6.6	100.0	−4.8	1.8	1.8	2.4
14–16	0.3	0.7	0.9	1.5	1.6	1.9	−4.8	100.0	−3.9	2.3	2.5
16–18	0.3	0.9	1.3	1.8	2.1	2.7	1.8	−3.9	100.0	−3.8	2.7
18–20	0.3	0.8	1.1	1.4	1.7	2.3	1.8	2.3	−3.8	100.0	−5.2
20–22	0.3	0.8	1.1	1.6	1.8	2.4	2.4	2.5	2.7	−5.2	100.0

TABLE XXV. Raw $B^- \to \omega(3\pi) \ell^- \bar{\nu}_\ell$ obtained from the two-dimensional fit, unfolded yields, efficiencies and partial branching fractions in bins of q^2.

Δq^2, GeV^2/c^2	N_{fit}	$N_{\mathrm{fit}}^{\mathrm{unfolded}}$	ε, 10^{-4}	$\Delta\mathcal{B}$, 10^{-6}
0–7	23.7 ± 6.3	24.4 ± 6.6	7.59 ± 0.24	22.8 ± 6.2
7–14	50.7 ± 9.2	51.5 ± 9.7	6.48 ± 0.20	56.5 ± 10.6
14–21	24.6 ± 7.8	23.1 ± 7.8	4.84 ± 0.22	33.9 ± 11.5
Full range	99.0 ± 15.0	99.0 ± 15.0	6.42 ± 0.14	113.3 ± 18.0

TABLE XXVI. Normalized statistical correlation matrix in percent for the $B^- \to \omega(3\pi) \ell^- \bar{\nu}_\ell$ partial branching fractions.

Δq^2, GeV^2/c^2	0–7	7–14	14–21
0–7	100.0	1.5	10.3
7–14	1.5	100.0	9.1
14–21	10.3	9.1	100.0

[1] N. Cabibbo, Phys. Rev. Lett. **10**, 531 (1963); M. Kobayashi and T. Maskawa, Prog. Theor. Phys. **49**, 652 (1973).

[2] The angle ϕ_1 is also referred to by the symbol β in the literature; similarly, $\phi_2 \equiv \alpha$ and $\phi_3 \equiv \gamma$.

[3] B. Aubert *et al.* (*BABAR* Collaboration), Phys. Rev. Lett. **87**, 091801 (2001); K. Abe *et al.* (Belle Collaboration), Phys. Rev. Lett. **87**, 091802 (2001).

[4] B. Aubert *et al.* (*BABAR* Collaboration), Phys. Rev. D **79**, 072009 (2009); I. Adachi *et al.* (Belle Collaboration), Phys. Rev. Lett. **108**, 171802 (2012).

[5] J. Beringer *et al.* (Particle Data Group), Phys. Rev. D **86**, 010001 (2012).

[6] Y. Ahmis *et al.* (HFAG Collaboration), arXiv:1207.1158.

[7] S. B. Athar *et al.* (CLEO Collaboration), Phys. Rev. D **68**, 072003 (2003); N. E. Adam *et al.* (CLEO Collaboration), Phys. Rev. Lett. **99**, 041802 (2007).

[8] P. del Amo Sanchez *et al.* (*BABAR* Collaboration), Phys. Rev. D **83**, 032007 (2011).

[9] P. del Amo Sanchez *et al.* (*BABAR* Collaboration), Phys. Rev. D **83**, 052011 (2011).

[10] B. Aubert *et al.* (*BABAR* Collaboration), Phys. Rev. Lett. **97**, 211801 (2006).

[11] B. Aubert *et al.* (*BABAR* Collaboration), Phys. Rev. Lett. **101**, 081801 (2008).

[12] J. P. Lees *et al.* (*BABAR* Collaboration), Phys. Rev. D **86**, 092004 (2012).

[13] H. Ha *et al.* (Belle Collaboration), Phys. Rev. D **83**, 071101(R) (2011).

[14] T. Hokuue *et al.* (Belle Collaboration), Phys. Lett. B **648**, 139 (2007).

[15] C. Schwanda *et al.* (Belle Collaboration), Phys. Rev. Lett. **93**, 131803 (2004).

[16] Charge-conjugate decays are implied throughout this paper.

[17] S. Kurokawa and E. Kikutani, Nucl. Instrum. Methods Phys. Res., Sect. A **499**, 1 (2003), and other papers included in this volume; T. Abe *et al.*, Prog. Theor. Exp. Phys. 03A001 (2013) and following articles up to 03A011.

[18] A. Abashian *et al.* (Belle Collaboration), Nucl. Instrum. Methods Phys. Res., Sect. A **479**, 117 (2002); also see detector section in J. Brodzicka *et al.*, Prog. Theor. Exp. Phys. 04D001 (2012).

[19] Z. Natkaniec *et al.* (Belle SVD2 Group), Nucl. Instrum. Methods Phys. Res., Sect. A **560**, 1 (2006).

[20] M. Feindt, F. Keller, M. Kreps, T. Kuhr, S. Neubauer, D. Zander, and A. Zupanc, Nucl. Instrum. Methods Phys. Res., Sect. A **654**, 432 (2011).

[21] J. D. Richman and P. R. Burchat, Rev. Mod. Phys. **67**, 893 (1995).

[22] E. Barberio and Z. Was, Comput. Phys. Commun. **79**, 291 (1994).

[23] P. Ball and R. Zwicky, J. High Energy Phys. 10 (2001) 019.

[24] P. Ball and R. Zwicky, Phys. Rev. D **71**, 014029 (2005).

[25] D. Scora and N. Isgur, Phys. Rev. D **52**, 2783 (1995); N. Isgur, D. Scora, B. Grinstein, and M. B. Wise, Phys. Rev. D **39**, 799 (1989).

[26] F. De Fazio and M. Neubert, J. High Energy Phys. 06 (1999) 017.

[27] T. Sjöstrand, P. Edén, C. Friberg, L. Lönnblad, G. Miu, S. Mrenna, and E. Norrbin, Comput. Phys. Commun. **135**, 238 (2001).

[28] C. Bourrely, I. Caprini, and L. Lellouch, Phys. Rev. D **79**, 013008 (2009).

[29] G.C. Fox and S. Wolfram, Phys. Rev. Lett. **41**, 1581 (1978); The modified moments used in this paper are described in S. H. Lee *et al.* (Belle Collaboration), Phys. Rev. Lett. **91**, 261801 (2003).

[30] K. Hanagaki, H. Kakuno, H. Ikeda, T. Iijima, and T. Tsukamoto, Nucl. Instrum. Methods Phys. Res., Sect. A **485**, 490 (2002).

[31] A. Abashian *et al.*, Nucl. Instrum. Methods Phys. Res., Sect. A **491**, 69 (2002).

[32] R. J. Barlow and C. Beeston, Comput. Phys. Commun. **77**, 219 (1993).

[33] A. Khodjamirian, Th. Mannel, N. Offen, and Y.-M. Wang, Phys. Rev. D **83**, 094031 (2011).

[34] P. Ball and R. Zwicky, Phys. Rev. D **71**, 014015 (2005).

[35] E. Gulez, A. Gray, M. Wingate, C. T. H. Davies, G. P. Lepage, and J. Shigemitsu, Phys. Rev. D **73**, 074502 (2006); **75**, 119906(E) (2007).

[36] J. A. Bailey *et al.*, Phys. Rev. D **79**, 054507 (2009).

[37] M. Beyer and D. Melikhov, Phys. Lett. B **436**, 344 (1998).

[38] L. D. Debbio, J. M Flynn, L. Lellouch, and J. Nieves (UKQCD Collaboration), Phys. Lett. B **416**, 392 (1998).

[39] A. Bharucha, J. High Energy Phys. 05 (2012) 092.

[40] http://ckmfitter.in2p3.fr/www/results/plots_ichep12/num/ckmEval_results.html.

[41] http://www.utfit.org/UTfit/ResultsWinter2013PreMoriond.